

Neutral Particle Identification in the $\overline{\text{PANDA}}$ Electromagnetic Calorimeter

Bachelor's Thesis in Physics

Author:
E. A. Dijck

Supervisor:
Dr. J. G. Messchendorp (KVI)

Abstract

In this work, several parameters are reviewed that can be used for the identification of signals in the electromagnetic calorimeter of the target spectrometer of the future $\overline{\text{PANDA}}$ detector. Specifically the problem of differentiating between clusters caused by single photons and clusters caused by two photons due to a neutral pion decay was investigated: at high momenta, neutral pions can decay into two photons with a small opening angle, resulting in overlapping signals that can be misinterpreted as single-photon clusters. Additionally, the effect of adding neutrons to the classification problem was investigated.

To benchmark the identification methods, a Monte Carlo simulation was performed using the PandaRoot software in development as part of the $\overline{\text{PANDA}}$ project. This showed that satisfactory separation between one-photon and two-photon clusters can be accomplished using a single shower shape parameter, the second cluster moment $\langle r^2 \rangle$. The classification efficiency hence obtained is better than that of the algorithm for handling multi-photon clusters currently implemented in PandaRoot. The classification efficiency that is ultimately achievable depends strongly on the momentum of the involved particles and the part of the detector that is being investigated.

KERNFYSISCH VERSNELLER INSTITUUT,
RIJKSUNIVERSITEIT GRONINGEN

December 2009

Contents

Introduction	4
1 The $\bar{\text{P}}\text{ANDA}$ experiment	6
1.1 The $\bar{\text{P}}\text{ANDA}$ project	6
1.2 The $\bar{\text{P}}\text{ANDA}$ detector	7
1.2.1 Target spectrometer	8
1.2.2 Forward spectrometer	11
2 Physics of the EMC	13
2.1 Annihilations	13
2.2 Particle showers	13
2.2.1 Electromagnetic showers	13
2.2.2 Hadronic showers	17
2.2.3 Material properties of the EMC	17
2.3 Neutral particles	17
2.3.1 Neutral pion decay	18
3 Computer simulations	20
3.1 PandaRoot	20
3.1.1 Monte Carlo simulations	21
3.2 EMC simulations	22
3.2.1 Digis	22
3.2.2 Clusters	23
3.2.3 Bumps	24
3.3 Examples	25
3.3.1 Clusters	25
3.3.2 Neutral pion opening angle	27
3.3.3 Energy loss	27
4 Cluster Parameters	29
4.1 General parameters	30
4.1.1 Energy loss	30
4.2 Bump parameters	30
4.2.1 Bump multiplicity	30
4.2.2 Invariant mass reconstruction	30
4.3 Shower shape parameters	31
4.3.1 Cluster energy fractions	31
4.3.2 Cluster mass	32

4.3.3	Cluster moments	32
4.3.4	Zernike moments	33
4.3.5	Eccentricity	35
5	Analysis	38
5.1	Data generation	38
5.1.1	EMC geometry considerations	38
5.1.2	Simulation parameters	41
5.1.3	Event selection	41
5.2	Analysis tools	43
5.2.1	Receiver Operating Characteristic curve	43
5.2.2	k -Nearest Neighbor algorithm	45
6	Results	49
6.1	Bump parameters	50
6.1.1	Bump multiplicity	50
6.1.2	Invariant mass reconstruction	52
6.1.3	Concluding remarks (bump parameters)	54
6.2	Shower shape parameters	54
6.2.1	Cluster energy fractions	54
6.2.2	Cluster mass	58
6.2.3	Cluster moments	60
6.2.4	Zernike moments	60
6.2.5	Eccentricity	64
6.2.6	Concluding remarks (shower shape parameters)	67
6.3	Multivariate analysis	68
6.4	Adding neutrons	69
6.4.1	Single parameters	70
6.4.2	Multivariate analysis	70
	Discussion and conclusions	72
	Bibliography	74
	A Additional data	75

Introduction

Recently work has started on the construction of a new facility for atomic, nuclear and particle physics at GSI in Darmstadt, Germany. One of the key experiments planned at this future Facility for Antiprotons and Ions Research (FAIR) is the $\overline{\text{P}}\text{ANDA}$ project.

$\overline{\text{P}}\text{ANDA}$ is an international collaboration with the aim of systematically studying the strong interaction. This interaction acts between quarks and is mediated via so-called gluons, which bind quarks together to form hadronic matter such as protons and neutrons, the building blocks of atomic nuclei. The exact nature of the strong interaction is still not well-understood on a quantitative level. Remarkable phenomena caused by this interaction are confinement, the impossibility of freely propagating quarks and gluons, and the generation of the hadron masses, as only a small part of the mass of hadrons can be accounted for by the constituent quarks.

The physics program of the $\overline{\text{P}}\text{ANDA}$ project covers various topics, particularly in hadron spectroscopy. The project will experimentally seek new forms of hadronic matter predicted by quantum chromodynamics that exist outside of the naive quark model. This includes so-called ‘glueballs’, exotic states of matter that consist only of gluons. Accurate measurements of the properties of particles containing charm quarks will also be carried out.

To perform the planned studies, the $\overline{\text{P}}\text{ANDA}$ experiment will use an accelerated beam of antiprotons interacting with various targets, including a hydrogen pellet target. The antiprotons will annihilate with the protons of the target and their combined energy will be converted into the hadronic matter of interest. All kinds of particles can be formed, mostly unstable, resulting in a decay chain generating a large set of more stable particles, such as photons and charged pions. To reconstruct the physical events that took place, the $\overline{\text{P}}\text{ANDA}$ experiment will include a detector capable of observing the particles created during the annihilation events. The design of the detector is well underway and the construction of the detector is scheduled to be completed in 2016.

In parallel to the design of the detector, computer simulations of the detector are being developed, to test the detector design and to provide a testbed for the analysis and interpretation of the data that the real detector will eventually provide. This software framework is used to simulate the response of the detector to various particles and also includes the analysis tools needed to study this data.

KVI in Groningen is a participating institute in the $\overline{\text{P}}\text{ANDA}$ collaboration. Alongside work on the $\overline{\text{P}}\text{ANDA}$ computer simulations, KVI is an important contributor to the design and testing of the electromagnetic calorimeter (EMC)

of the $\overline{\text{PANDA}}$ detector and its read-out electronics.

The EMC of the $\overline{\text{PANDA}}$ detector consists of a large number of scintillation crystals designed to detect particles passing through, primarily photons, electrons and positrons. When a particle strikes the EMC, it will form a ‘shower’ of secondary particles. These secondary particles will be absorbed in the crystals and produce scintillation photons, which are measured to reconstruct the energy of the incident particle. An important property of the EMC is that it can detect both charged and neutral particles, while most of the other parts of the $\overline{\text{PANDA}}$ detector detect only charged particles. The identification of neutral particles is therefore an important task of the EMC.

Amongst the neutral particles that will be created in large numbers during the annihilation events in the $\overline{\text{PANDA}}$ detector are photons and neutral pions. This last type of particle is unstable and decays immediately into mostly two photons. If the opening angle between the two photons is small, the showers generated by both photons overlap and the signal they give in the EMC can easily be misinterpreted as a signal stemming from a single photon. The goal of this thesis is to review methods of identifying photons and neutral pions based on the signal they produce in the EMC. To achieve this, the shape of their showers in the EMC is analyzed, using various parameters that quantify the differences between one-photon and two-photon events. To test the performance of these parameters, computer simulations of the $\overline{\text{PANDA}}$ detector were extensively used.

As will be shown in this thesis, good results can be obtained for the separation between photons and neutral pions in the $\overline{\text{PANDA}}$ EMC by using a single well-chosen shower shape parameter or a combination of a small number of these. Additionally, it will be shown that adding neutrons, another class of neutral particles, to the classification problem will not drastically change which parameters perform well in classification. Neutrons produce very irregular showers in the EMC and these can be distinguished from photon showers by most shower shape parameters.

The outline of the thesis is the following. Some general information about the design of the $\overline{\text{PANDA}}$ detector will be given in Chapter 1, as well as a description of the design of the EMC subdetector. Chapter 2 will treat the physical processes that are relevant for this thesis. A discussion of the $\overline{\text{PANDA}}$ computer simulation and analysis framework will be given in Chapter 3. In the following chapters, the analysis done for this thesis will be described. In Chapter 4, the shower shape parameters that have been investigated for their classification power will be presented. Chapter 5 deals with the methods that were used for generating and analyzing data for this thesis. Finally, Chapter 6 will show the results of this analysis. From these results some conclusions will be drawn regarding the best method for identifying photons and neutral pions in the EMC of the $\overline{\text{PANDA}}$ detector.

Elwin Dijck – e.a.dijck@student.rug.nl

Chapter 1

The $\bar{\text{P}}\text{ANDA}$ experiment

In this first chapter, some background information about the $\bar{\text{P}}\text{ANDA}$ experiment and the corresponding yet-to-be-built detector will be given. In particular the electromagnetic calorimeter of the detector will be described, since this is the part of the detector that was investigated during this project.

1.1 The $\bar{\text{P}}\text{ANDA}$ project

The Antiproton Annihilations at Darmstadt ($\bar{\text{P}}\text{ANDA}$) experiment that will take place in the near future will be used to perform strong interaction studies using an accelerated beam of antiprotons and various targets. This will take place at the future Facility for Antiproton and Ion Research (FAIR) at the GSI Helmholtz Center for Heavy Ion Research (GSI) at Darmstadt, Germany. The $\bar{\text{P}}\text{ANDA}$ experiment is one of several experiments that will take place at this new accelerator facility, as depicted in Figure 1.1

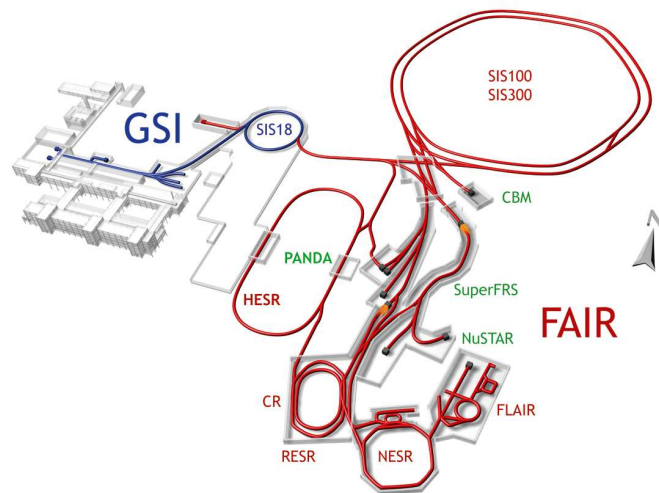


Figure 1.1 – Overview of existing accelerators at GSI (in blue) and the future FAIR facility (in red) with the various experiments (in green). [1, Fig. 2.1]

The experiment has a broad physics program that will focus on hadron spectroscopy, to study for instance processes involving charmed hadrons or the search for the theoretically predicted states of matter called *glueballs*. Using the future High-Energy Storage Ring (HESR) and the (upgraded) existing accelerator facilities at GSI, it will be possible to produce high-quality antiproton beams with a momentum of up to 15 GeV/c.

The $\bar{\text{P}}\text{ANDA}$ project is an international collaboration established in 2002 in which more than 400 scientists from 16 countries and 53 institutions are involved in the development of the required hardware and software. It is expected that the experiment will start its operation in 2016. To aid in the design of the detector hardware and software, a computer simulation of the detector and data-analysis framework has been in development since 2006. This software was used extensively during this project and will be treated in detail in Chapter 3. For a more extensive introduction to the $\bar{\text{P}}\text{ANDA}$ project and its physics program, see [2, p. 13–29] or [3, p. 1–10].

1.2 The $\bar{\text{P}}\text{ANDA}$ detector

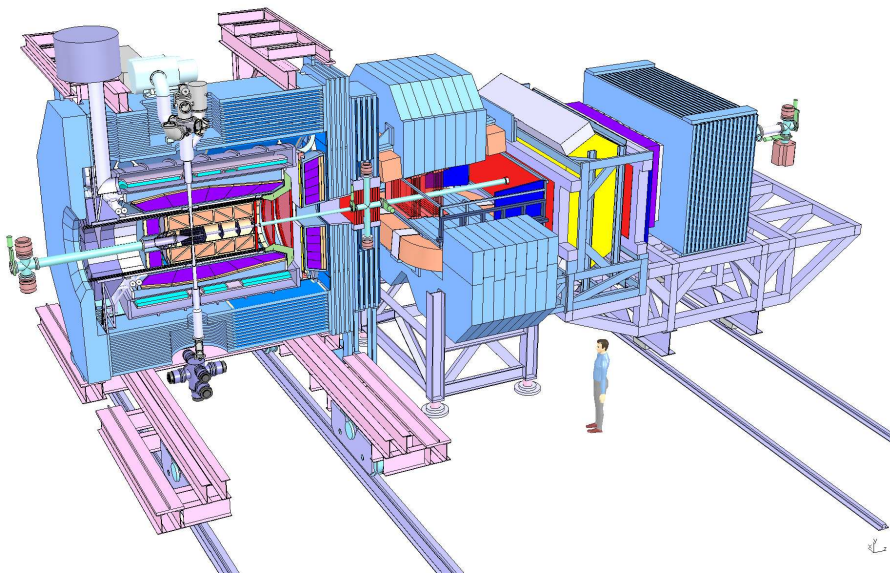


Figure 1.2 – Overview of the $\bar{\text{P}}\text{ANDA}$ detector with the target spectrometer to the left and the forward spectrometer to the right. The anti-proton beam enters from the left. [1, Fig. 1]

The detector that will be built at FAIR for the $\bar{\text{P}}\text{ANDA}$ experiment is currently in the final stages of its design. Its main objectives are to achieve almost full 4π angular acceptance and a high resolution for tracking, particle identification and calorimetry, while being capable of handling high event rates in the order of 10^7 s^{-1} .

The detector consists of two main parts (see Figure 1.2): the *target spectrometer* located around the target, where the interactions with the antiproton

beam will take place, and the *forward spectrometer* for particles which exit the target area with a small angle with respect to the beam direction. In both parts, tracking, charged particle identification, calorimetry and muon identification are available. To achieve this, both parts consist of several subdetectors that will be succinctly described in the next sections. For this thesis, the response to neutral particles of the electromagnetic calorimeter in the target spectrometer was investigated, and this subdetector will receive extra attention.

1.2.1 Target spectrometer

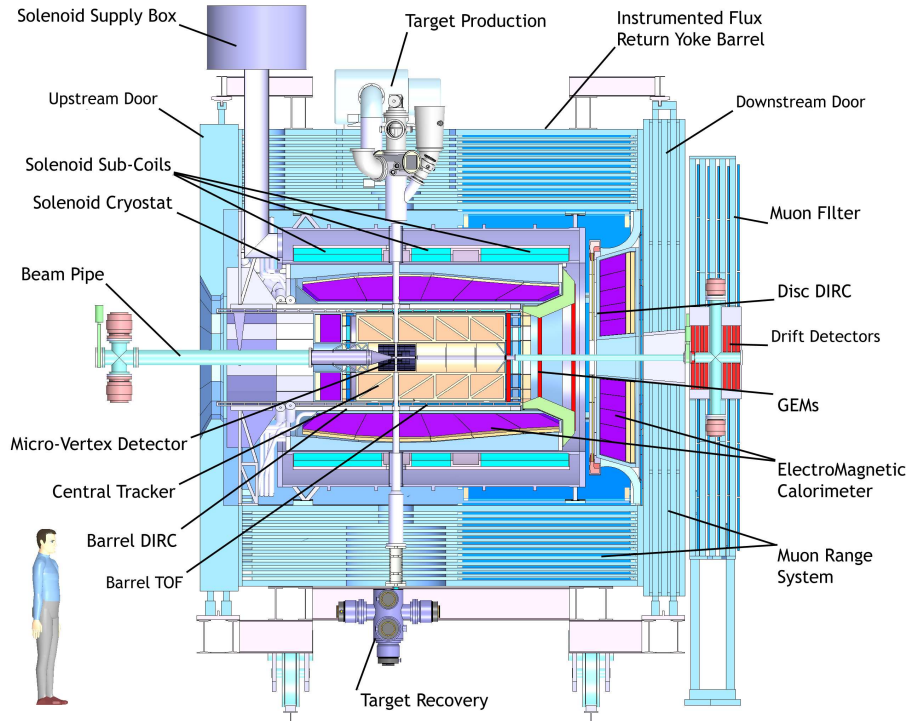


Figure 1.3 – Cross-sectional side view of the target spectrometer part of the $\overline{\text{P}}\text{ANDA}$ detector with the major components marked. The modules of the electromagnetic calorimeter are colored purple. [1, Fig. 2.5]

The target spectrometer (see Figure 1.3) surrounds the interaction point of the antiproton beam with the target and consists of layers of subdetectors in a compact ‘onion shell’ configuration. The target spectrometer is enclosed by a superconducting solenoidal magnet producing a magnetic field of about 2 T. It contains, amongst others, the following instruments:

Target Several types of targets are foreseen during the experiments. These include a *cluster-jet target*, where pressurized cold hydrogen gas is injected into the beam, and a *pellet target*, where micro-spheres of frozen hydrogen are shot into the beam. Other types of target that can accommodate nuclei of heavier elements are under consideration.

Micro-vertex Detector (MVD) The MVD surrounds the target and detects secondary decays of charmed or strange particles displaced from the primary interaction point.

Straw Tube Tracker (STT) The STT surrounds the MVD and is the primary tracker of the target spectrometer, consisting of several thousand gas-filled tubes that can detect charged particles passing through.

Time Projection Chamber (TPC) The TPC is an alternative to the STT which uses two large gas-filled chambers to track charged particles. Either the STT or the TPC will be installed in the \bar{P} ANDA detector.

Detector for Internally Reflected Cherenkov light (DIRC) The DIRC uses Cherenkov light to detect charged particles with high velocities and consists of a barrel part and a forward end-cap. It is used for particle identification, especially the differentiation between pions and kaons.

Electromagnetic Calorimeter (EMC) The EMC is a calorimeter for detecting particles interacting via electromagnetic processes. Its primary use will be the identification of electrons and positrons, and neutral particles like photons.

Muon detectors Interleaved with the yoke of the magnet, this subdetector consists of tracking detectors for the detection of muons, either created at the target or from decays of other particles.

During the experiments, information from the various subdetectors will be combined to identify all particles created during an event and to reconstruct the physical processes that took place.

Electromagnetic Calorimeter

An electromagnetic calorimeter is primarily designed to detect particles that interact via electromagnetic processes, most importantly photons, electrons and positrons. The EMC of the target spectrometer is designed to be compact to fit into the magnet and to have a fast response time to cope with the planned high event rates. It is the only subdetector able to reliably identify neutral particles, since these have little or no interaction with most subdetectors.

In this thesis, the classification of different types of neutral particles by using the information from the EMC of the \bar{P} ANDA detector is studied. Although the EMC is mainly designed for the detection of photons, it can also be used for the identification of neutral hadrons, like neutrons.

The EMC of the target spectrometer consists of the following three modules:

- the cylindrical *barrel*, covering the directions between about 20° and 150° from the beam direction;
- the *forward end-cap*, covering the directions between about 5° in the vertical plane and 10° in the horizontal plan to 20° from the beam direction;
- and the *backward end-cap*, covering the directions between about 150° and 170° from the beam direction.

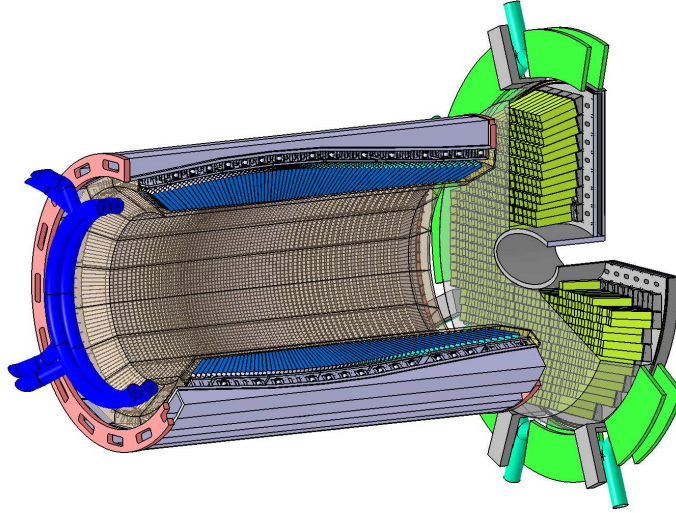


Figure 1.4 – Cut-away drawing of the electromagnetic calorimeter of the target spectrometer with holding structures and coolant pipes. Shown is the barrel module (left) and the forward end-cap (right). The modules are cut open to provide a better view of the inside. The transparent cover over the crystals is the insulation to help keep them at their working temperature of -25°C . [2, Fig. on cover]

Each module of the EMC consists of a large number of lead–tungstate (PWO-II) scintillation crystals, totaling about 17 000. The crystals are approximately rectangularly box-shaped, with a front face of about 2 cm by 2 cm and a length of 20 cm. The crystals all face the target position, with a small aberration to prevent the possibility that particles travel through the small spaces between the crystals needed for their holding structure and cooling. Apart from particles that move through the hole in the forward end-cap, which will be detected by the forward spectrometer, this design provides an acceptance of almost the full solid angle.

Particles interact with the EMC by forming *particle showers*, which will be described in more detail in Section 2.2 along with some of the physical processes involved. During these showers, scintillation photons are produced in the crystals, which will be converted to electric signals by, depending on the module, either Avalanche Photodiodes (APDs) or Vacuum Phototriodes (VPTs) [2, p. 67–84]. This provides a measure of the energy of all photons formed in a single crystals and corresponds to the raw data that the EMC provides, e.g. the deposited energy in each crystal as a function of time.

Since the EMC of the target spectrometer has only a single layer of crystals as seen from the target, no information about the depth profile of particle showers is preserved, as would be the case for sampling calorimeters such as the electromagnetic calorimeter of the ATLAS detector at CERN [4]. The data the EMC gives can thus be described as the deposited energy as a function of direction from the target and time.

In Section 2.2.3 some more information will be given about the relevant material properties of the crystals of the EMC.

1.2.2 Forward spectrometer

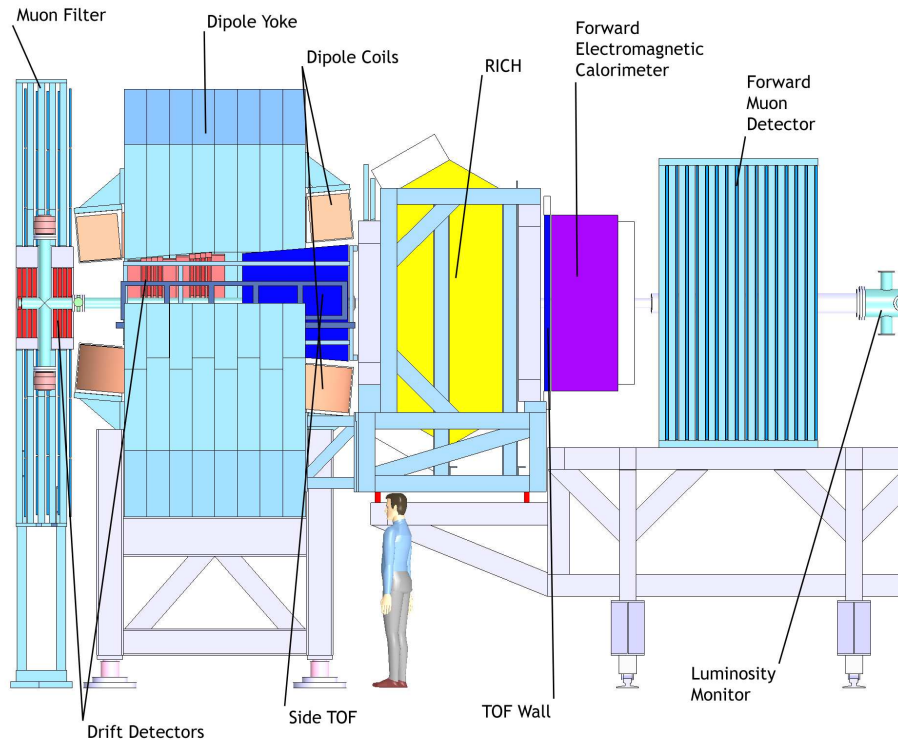


Figure 1.5 – Side view of the forward spectrometer part of the \bar{P} ANDA detector with the major components marked. [1, Fig. 2.10]

The forward spectrometer is designed to detect particles that leave the target position at small angles from the beam direction. It fully covers the forward angular acceptance of $\pm 10^\circ$ in the horizontal direction and $\pm 5^\circ$ in the vertical direction. The forward spectrometer is enclosed by a dipole magnet and contains mostly the same types of subdetectors that the target spectrometer has, including the following:

Forward trackers The forward trackers will consist of wire chambers, straw tubes and/or Gas Electron Multiplier (GEM) detectors to measure the deflection of charged particle trajectories in the field of the dipole magnet.

Ring Imaging Cherenkov (RICH) detector The RICH is a Cherenkov detector for detecting high-velocity particles to enable the separation between protons, pions and kaons.

Time-of-Flight (TOF) wall This is a wall made of scintillation material to supply a time measurement for calculating the (relative) flight times of particles.

Electromagnetic Calorimeter (EMC) The EMC of the forward spectrometer is a ‘shashlik-type’ electromagnetic calorimeter to detect photons,

electrons and positrons. Its purpose is similar to that of the EMC of the target spectrometer, but it is a sampling calorimeter and consists of a different scintillation material alternated with lead.

Hadron calorimeter Located behind the forward electromagnetic calorimeter, this calorimeter is designed specifically to detect hadrons.

Forward muon detectors The forward spectrometer contains muon detectors similar to the ones in the target spectrometer, but designed for particles with higher momenta.

During this project only the response of the EMC of the target spectrometer was investigated, but some of the concepts treated might also apply to the EMC of the forward spectrometer. When referring to the ‘EMC’ in this thesis, only the EMC of the target spectrometer will be meant.

Chapter 2

Physics of the EMC

2.1 Annihilations

During the $\bar{\text{P}}\text{ANDA}$ experiment, a beam of antiprotons with momenta of up to 15 GeV/ c will interact with various targets. This results in the annihilation of antiprotons of the beam with protons of the target, converting their mass into energy. Depending on the beam energy, a host of different types of elementary and hadronic particles can be formed, such as electrons, pions, kaons, neutrons, etc. In this thesis the focus lies on the neutral particles that will be described in Section 2.3. These particles do not interact with most subdetectors of the $\bar{\text{P}}\text{ANDA}$ detector, but they do interact with the electromagnetic calorimeter in a way that will also be described.

To study the response of the $\bar{\text{P}}\text{ANDA}$ EMC, it is not needed to simulate full annihilation events, and during this project the particles of interest were simulated separately from each other. Thus except for noting that all particles considered in this thesis can be created during antiproton–proton annihilations, the underlying reaction mechanisms will not be discussed any further.

2.2 Particle showers

When a high-energy particle enters dense matter, it will be slowed down by various interactions with the atoms of the material. During these processes, multiple secondary particles are formed, each possibly forming further particles, resulting in a ‘shower’ of particles. These showers can be subdivided into two basic types, depending on the type of the initiating particle: electromagnetic and hadronic showers.

2.2.1 Electromagnetic showers

High-energy photons and electrons, or other particles that interact primarily via the electromagnetic force, form an *electromagnetic shower* when entering a dense material. Several processes will take place depending on the type and energy of the incoming particle. In this section the processes that will successively take place when a high-energy photon enters matter will be described [5, p. 128–130].

Pair production

At high energies (above a few MeV), the primary interaction of photons with matter is the pair production process: a photon is converted into a pair of an electron and its antiparticle, a positron. This process would not conserve both momentum and energy in vacuum, but it is possible in the vicinity of a nucleus (or atomic electrons) when the photon is traversing a material, as these can absorb the excess momentum.

Since the electron and positron have a rest mass of $m_e = 511 \text{ keV}/c^2$, the pair production process is possible for photons with an energy of at least the threshold energy of 1.02 MeV. Additional energy of the photon is converted into kinetic energy, distributed over the electron-positron pair.

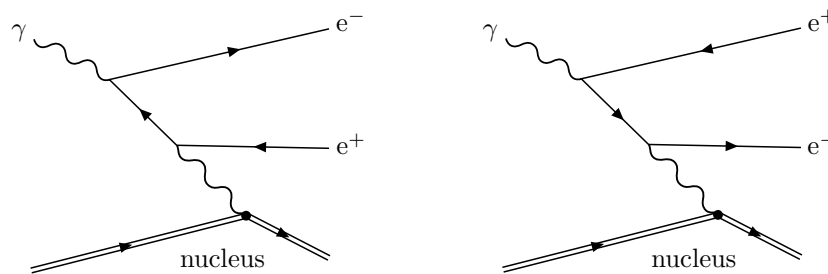


Figure 2.1 – Dominant Feynman diagrams of the electron-positron pair production process [5, Fig. 4.11].

Bremsstrahlung

High-energy electrons and positrons interact primarily with matter via bremsstrahlung, a process whereby the charged particle is deflected in the electric field of a nucleus and a photon is emitted. The electron or positron is first accelerated and then decelerated in the process, causing it to radiate a photon.

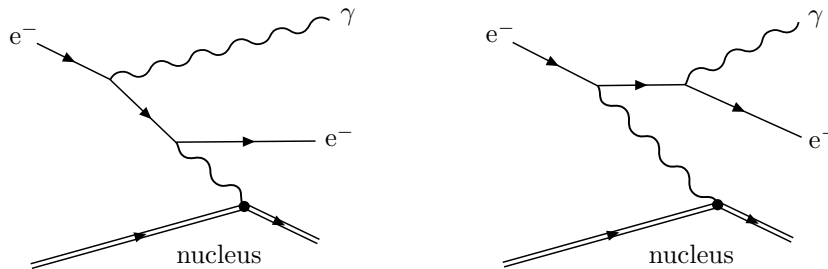
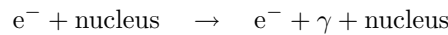


Figure 2.2 – Dominant Feynman diagrams of the bremsstrahlung process for an electron [5, Fig. 4.9].

In an electromagnetic shower, the dominant process for photons is the pair production process, and the dominant process for electrons and positrons is the bremsstrahlung process. While the energy of the particles is sufficiently high, the pair production and bremsstrahlung processes alternate, producing a large number of particles (see Figure 2.3). After the particles have lost most of their energy through these processes, they will scatter and finally be absorbed by atoms of the material in ionization processes or, in the case of positrons, annihilate with atomic electrons, producing new photons.

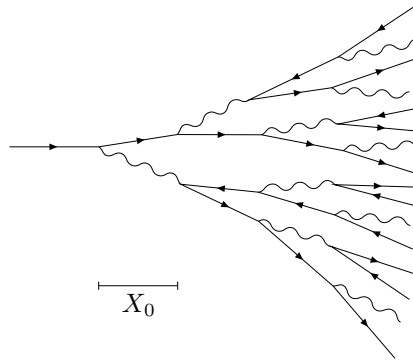


Figure 2.3 – A diagram of the start of an electromagnetic shower initiated by an electron, depicting approximately four radiation lengths [5, Fig. 4.17].

At low energies (below a few MeV), the main interactions of photons with matter are the photoelectric effect and Compton scattering. The first process involves the absorption of a photon by an atomic electron, where the electron is subsequently ejected from the atom. The atomic nucleus absorbs the recoil momentum. This process dominates at the lowest photon energies, but its cross section rapidly falls with increasing energy. In the Compton scattering process, photons are scattered from atomic electrons, or from all the electrons of an atoms as a whole (coherent or Rayleigh scattering). The cross section of the pair-production process rises rapidly from its threshold energy of 1.02 MeV and is the dominant process at high energies [6, p. 53–59].

Longitudinal shower shape

While an electromagnetic shower develops, the number of particles in the shower increases approximately exponentially with depth until it reaches a maximum when the particle energies are of the order of the *critical energy* E_c . The critical energy corresponds to the energy at which the energy loss of electrons from ionization equals the energy loss from bremsstrahlung. The longitudinal dimension of the shower is determined by the *radiation length* of the material, X_0 . The radiation length is the average thickness that reduces the energy of an electron by a factor of e . The values of these material properties for the lead–tungstate crystals of the $\overline{\text{PANDA}}$ EMC will be later given in a table.

Although the development of an electromagnetic shower is a statistical process, the general shape of a shower can be described by using a very simple model consisting of the following rules [5, p. 143–145] [6, p. 59–60]:

- electrons or positrons with an energy larger than E_c travel one radiation length after which they radiate half their energy via bremsstrahlung photons;
- photons with an energy larger than E_c travel one radiation length after which they create electron–positron pairs, with their energy equally divided over these two particles;
- ionization losses are negligible for particles with an energy above E_c .

In this model, the number of particles in the shower doubles after each radiation length. At any point in the shower, the number of photons, electrons and positrons is approximately equal and all particles have the same energy. For an initial electron, positron or photon with an energy of $E_0 \gg E_c$, the number of particles as a function of depth X is given by

$$N(t) = 2^t, \quad \text{where } t = \frac{X}{X_0},$$

and each particle at a certain depth has an energy of

$$E(t) = E_0 \cdot 2^{-t}.$$

The multiplication of particles will suddenly stop when $E(t) = E_c$, where the number of particles in the shower has reached its maximum. It follows that this happens at a depth of

$$X_{\max} = X_0 \cdot \frac{\ln(E_0/E_c)}{\ln 2},$$

and the maximum number of particles produced is

$$N_{\max} = \frac{E_0}{E_c}.$$

Although this model is a simplification of the process, the important observation that the shower depth depends logarithmically on the energy of the primary particle is observed experimentally. In reality, the number of particles in an electromagnetic shower rises exponentially to a relatively broad maximum, after which it declines gradually, instead of abruptly as in the model treated above [6, p. 60].

Lateral shower shape

While an electromagnetic shower develops, its transverse dimensions also increase due to the finite opening angle between the electron and positron in the pair production process, multiple scattering of the electrons and the emission of bremsstrahlung photons away from the shower axis. The lateral dimensions of showers can be measured in terms of the *Molière radius* of the material, R_M . The lateral energy distribution of an electromagnetic shower decays mainly exponentially, with more than 90% of the energy of the shower deposited within a distance of about $2R_M$ from the shower axis [6, p. 61].

2.2.2 Hadronic showers

When high-momentum hadrons, such as neutrons, enter a dense material, they also form showers of secondary particles. These *hadronic showers* are qualitatively similar to electromagnetic showers, but several different types of hadrons are formed in these showers and this makes them far more complex to describe than the electromagnetic showers treated in the previous section. Many different processes contribute to the inelastic production of secondary hadrons.

The cross sections of most interactions of hadrons with matter are typically smaller than the cross sections of the electromagnetic processes treated earlier, because they are due to the short-range strong force. This holds especially for neutral hadrons such as neutrons, which do not interact via the electromagnetic force at all.

Several possible hadronic interactions also produce photons, electrons or positrons, and if these particles have sufficient energy, they will form a secondary electromagnetic shower. Thus hadronic showers will in general also be partly electromagnetic in character [5, p. 145]. Because of the small interaction cross sections, neutrons are very penetrating particles and in general only part of their energy will be deposited in the EMC.

2.2.3 Material properties of the EMC

A calorimeter detects particles by measuring the deposited energy of the secondaries from the electromagnetic shower that is created when a particle enters the detector. The lead–tungstate material chosen for the crystals of the $\overline{\text{P}}\text{ANDA}$ electromagnetic calorimeter has a short radiation length to allow for a compact detector design (see the table below). The crystals have a length of 20 cm, corresponding to about 22 radiation lengths, which allows good shower containment for photons with energies of up to 15 GeV. The simple model treated before predicts that for a photon of 15 GeV, the shower maximum would lie approximately half-way the crystal.

The table below gives the material properties that describe the dimensions of electromagnetic showers for the crystal material of the $\overline{\text{P}}\text{ANDA}$ EMC. The critical energy E_c is related to the radiation length and Molière radius as

$$E_c = \frac{X_0}{R_M} E_s,$$

where E_s is the scale energy given by $E_s = m_e c^2 \sqrt{4\pi/\alpha} = 21.2$ MeV [6, p. 61].

Material property	PWO-II value [2, Table 4.1]
density, ρ	8.28 g/cm ³
radiation length, X_0	0.89 cm
Molière radius, R_M	2.00 cm
critical energy, E_c	9.4 MeV

2.3 Neutral particles

During the annihilation events of the $\overline{\text{P}}\text{ANDA}$ experiment, different types of particles will be created, both at the target and from secondary decays. Correctly identifying these particles is thus important to be able to reconstruct the

complete reaction. In this thesis only stable neutral particles are studied. Most subdetectors of the PANDA detector only detect charged particles.

The track reconstructions from the inner detectors of the target spectrometer allow matching the particle showers in the EMC to charged particle tracks. Showers in the EMC which do not correspond to such tracks are likely to be caused by neutral particles. Thus the charge of the particles forming showers in the EMC is assumed to be known in this project, validating the approach of only investigating neutral particles.

The particle types that were studied during this project are *single photons*, photons originating from *neutral pions* ($m_{\pi^0} = 134.98 \text{ MeV}/c^2$) and *neutrons* ($m_n = 939.57 \text{ MeV}/c^2$) [7]. Of these three types of particles, especially the photons and neutral pions will be created in large numbers during the PANDA experiment. In this thesis, the ways of distinguishing their signals in the EMC are investigated.

2.3.1 Neutral pion decay

The neutral pion has a very short mean lifetime of $\tau = 8.4 \cdot 10^{-17} \text{ s}$ and decays due to the electromagnetic force. Its two largest decay modes are [7]:

$$\begin{aligned} \pi^0 &\rightarrow 2\gamma && (98.8\%) \\ \pi^0 &\rightarrow e^+ + e^- + \gamma && (1.2\%) \end{aligned}$$

Most pions decay into two photons, with about one percent decaying via the so-called *Dalitz decay* into an electron–positron pair and a photon, excluding further decay modes with branching ratios $\ll 1\%$. This thesis focusses on the first decay mode of the pion, as that is by far the largest decay mode and can produce characteristic two-photon detections in the EMC, while the pions that decay via the Dalitz decay are more difficult to reconstruct. The neutral pions themselves will never reach the EMC detector.

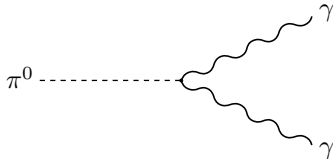


Figure 2.4 – A sketch of a neutral pion decaying into two photons.

The short lifetime of the neutral pion dictates that neutral pions that are created during an annihilation event decay within a very short distance of the target, $\tau c \approx 25 \text{ nm}$. Note, however, that neutral pions can also be formed further away from the target in secondary decays of relatively long-living unstable particles like, for example, kaons. Most neutral pions thus give rise to two separate electromagnetic showers in the EMC. From the conservation of energy and momentum laws, an expression for the minimum angle between the two emitted photons for a pion of energy E and momentum p can be derived¹,

$$E = E_{\pi^0} = E_{\gamma_1} + E_{\gamma_2} \quad \text{and} \quad \mathbf{p}_{\pi^0} = \mathbf{p}_{\gamma_1} + \mathbf{p}_{\gamma_2}, \quad \text{with} \quad p = \|\mathbf{p}_{\pi^0}\|. \quad (2.1)$$

¹Vector quantities are denoted by bold-face symbols.

Applying the law of cosines to the momentum conservation relation, one obtains the following expression for the angle θ between the two emitted photons:

$$\|\mathbf{p}_{\pi^0}\|^2 = \|\mathbf{p}_{\gamma_1}\|^2 + \|\mathbf{p}_{\gamma_2}\|^2 - 2\|\mathbf{p}_{\gamma_1}\|\|\mathbf{p}_{\gamma_2}\|\cos(\pi - \theta),$$

which can be rewritten in terms of energies as

$$E_{\pi^0}^2 - m_{\pi^0}^2 c^4 = E_{\gamma_1}^2 + E_{\gamma_2}^2 + 2E_{\gamma_1}E_{\gamma_2}\cos\theta.$$

Using conservation of energy from (2.1), this gives

$$\frac{m_{\pi^0}^2 c^4}{2E_{\gamma_1}E_{\gamma_2}} = 1 - \cos\theta. \quad (2.2)$$

As can be seen from expression (2.2), θ does not have a single solution (except when $p = 0$), but the angle depends on how the energy of the pion is divided between the two photons. Solving for the minimum and maximum angles as a function of momentum shows that

$$\theta_{\min}(p) = \cos^{-1}\left(1 - \frac{2m_{\pi^0}^2 c^2}{m_{\pi^0}^2 c^2 + p^2}\right) \quad \text{and} \quad \theta_{\max} = \pi. \quad (2.3)$$

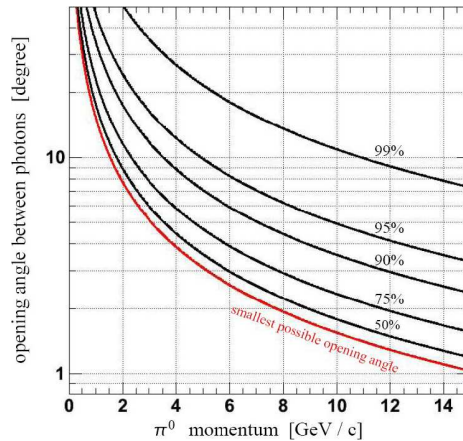


Figure 2.5 – Statistical distribution of the opening angle of decaying neutral pions as a function of momentum [2, Fig. 3.5].

Although expression (2.3) shows that large opening angles are possible at any momentum, the majority of the pion decays have opening angles close to the minimum, where the energy of the pion is divided evenly over the two photons (see Figure 2.5). This means that, in general, the opening angle will be small for high-momentum pions.

The photons due to the decay of a high-momentum pion will hit the electromagnetic calorimeter of the $\overline{\text{P}}\text{ANDA}$ detector at almost the same location and their electromagnetic showers may partly overlap. Therefore, some technique is needed to distinguish between the signals of single photons in the EMC and the signal of two photons close together. In the rest of this thesis, this separation analysis will be described and the results of testing the corresponding methods with the computer simulation of the $\overline{\text{P}}\text{ANDA}$ detector will be given.

Chapter 3

Computer simulations

To test the performance of the detector concept and to design the analysis algorithms that will eventually be used during the real experiments, a computer simulation of the $\overline{\text{P}}\text{ANDA}$ detector has been in development since 2006. The first stable release of the simulation framework was released in 2007. This simulation was used to obtain all data for this project and will be described in detail in this chapter, in particular the parts pertaining to the EMC.

The simulation can clearly not be used to study new physics as a replacement of the real experiment. However, it can certainly be used to study the response of the various parts of the $\overline{\text{P}}\text{ANDA}$ detector to known (or predicted) particles and reactions, as is done in this project. This information is needed to be able to correctly reconstruct the events that will take place in the $\overline{\text{P}}\text{ANDA}$ detector when it starts operating.

3.1 PandaRoot

The simulation for $\overline{\text{P}}\text{ANDA}$ is based on the ROOT framework² developed at CERN. ROOT is an open-source *object-oriented* framework providing a wide range of tools for doing (particle physics) data analysis, such as tools for histogramming, statistical data analysis and curve fitting. ROOT is written in the programming language C++ and has been in continuous development since 1994.

The simulation for $\overline{\text{P}}\text{ANDA}$ is called PandaRoot and is used for both the simulation and analysis of data. It is written in C++ and is one of several projects built on the FairRoot³ framework, a generic framework for the computer simulations of the various experiments planned at FAIR, primarily the $\overline{\text{P}}\text{ANDA}$ experiment, the Compressed Baryonic Matter (CBM) experiment and the Reactions with Relativistic Radioactive Beams (R³B) experiment. PandaRoot consists of several libraries that provide the functionality to simulate and analyze data for the $\overline{\text{P}}\text{ANDA}$ experiment.

²<http://root.cern.ch/>

³<http://fairroot.gsi.de/>

3.1.1 Monte Carlo simulations

The type of simulation used in PandaRoot is a *Monte Carlo simulation*: it relies on (pseudo-)random sampling of the probability distribution functions of the physical processes to be simulated. This type of simulation allows obtaining the full information about the trajectories and interactions of all particles that were created during the simulation. Because the ‘real’ events that took place in the simulation are known, such a simulation is ideally suited to study the response of the PANDA detector to certain types of events and investigate how the data from the detector should be interpreted.

Transport model

The part of PandaRoot that performs the actual simulation of physical processes is called the *transport model*, as it simulates the propagation of particles through matter. PandaRoot uses the *Virtual Monte Carlo* system of ROOT to decouple the transport model used from the rest of the simulation. This allows easy switching between the currently supported transport models, including amongst others GEANT3⁴ and Geant4⁵, both developed primarily at CERN. GEANT3 is written in FORTRAN and it was in development between 1974 and 1994, with some more recent releases containing bug fixes. Geant4 is its successor, rewritten in C++ and in development since 1998.

For this project, GEANT3 was used, as it is well-tested, somewhat faster than Geant4 and in this project only a comparison is made between the particle classes described in Section 2.3 and no quantitative measurements are done. Also, the electromagnetic processes that were of most importance for this project are well-known and therefore their implementation in GEANT3 should not differ much from Geant4.

Event generator

Apart from the detector geometry provided by PandaRoot, the transport model also requires an event generator to generate the particles it uses as input. The PandaRoot simulation allows the selection of various event generators, ranging from simple ones that generate single particles to more advanced generators that simulate, for instance, specific decay channels of a proton–antiproton annihilation or background radiation.

For this thesis, no antiproton–proton annihilations were simulated. Instead, single particles that could be formed during such an annihilation event were simulated separately from each other to observe the response they would produce in the EMC subdetector. To achieve this, a *box generator* was used that generates single particle events with uniformly distributed momenta $p \in [p_{\min}, p_{\max}]$ and directions $\theta \in [\theta_{\min}, \theta_{\max}]$, $\phi \in [\phi_{\min}, \phi_{\max}]$ at position (x, y, z) .

Coordinate system

The PandaRoot simulation uses a coordinate system where the origin is placed at the target position. To define a direction from the target, e.g. for specifying the direction of particles, the polar angle θ and azimuthal angle ϕ are used, where

⁴<http://wwwasd.web.cern.ch/wwwasd/geant/>

⁵<http://www.geant4.org/>

these are defined such that $x = r \sin \theta \cos \phi$, $y = r \sin \theta \sin \phi$ and $z = r \cos \theta$, with $r = \sqrt{x^2 + y^2 + z^2}$. The detector geometry is oriented such that the beam direction is in the positive z -direction, and θ gives the angle with respect to the beam direction.

Macros

To steer the simulation, macro files are used, which are written in C++ and interpreted by the CINT interpreter integrated in ROOT. It is also possible to compile the macros as normal C++ programs using the ACLiC compiler supplied with ROOT or using an external compiler. This last possibility was mainly used during this project, using the GNU C++ compiler⁶.

3.2 EMC simulations

As described before, the transport model calculates the trajectories of the generated particles and their interaction with the material of the various detectors defined in PandaRoot. Whenever a particle interacts with matter, the information about the amount of energy lost and any new particles that are created is stored. This raw interaction data then needs to be ‘digitized’ to obtain a realistic response of the subdetectors, including simulating their electronics, since this will be the only information available during the real experiments.

For the EMC subdetector, the steps for the simulation and digitization of a single event before further analysis are as follows:

- generation of particles by the event generator;
- simulation of the particles and their interactions with matter by the transport model, producing so-called *Monte Carlo points*;
- accumulation of all Monte Carlo points within a single crystal of the EMC into a *hit*;
- conversion of the hits into electric *waveforms* simulating the detector electronics;
- simulation of digitization of the waveforms to obtain digitized detector responses, so-called *digis*.

3.2.1 Digis

At this point the digis, the digitized responses of all individual crystal detectors, will be known and this concludes the simulation and digitization phase. Note that here the energy deposited in each of the EMC crystals is integrated over all time, which is possible since only a single event is simulated during each run of the simulation. In the actual experiment, the rate of events can be very high and some way of separating multiple particles striking the same crystal sequentially will be needed. This so-called pile-up correction is a task of the detector electronics. In this thesis it is assumed that this can be done reasonably well and thus it is valid to analyze all events separately. Note that it is not

⁶<http://gcc.gnu.org/>

possible to separate the two photons of a neutral pion decay by their time of impact, since they reach the EMC near-simultaneously.

The information from the digis is the starting point for the analysis described in this thesis. Note that this data can be represented as a two-dimensional grid of elements indexed by θ and ϕ , each containing the deposited energy in a single detector.

3.2.2 Clusters

A *cluster* is an iterative set of neighboring EMC crystals, each of which had a non-zero amount of energy deposited in it. As the crystals are laid out in a rectangular grid, each crystal typically has eight neighbors, except those at the edges of the detector modules.

Because neutral pions decay at the target mainly into two photons, as described in Section 2.3.1, and the angle between the two photons will generally be small at high momenta, so-called ‘merged clusters’ consisting of the electromagnetic showers of both photons can be formed. If the opening angle between the two photons due to a neutral pion decay is sufficiently large, then the two photons will form two separate clusters instead. In this last case, the two clusters are indistinguishable from clusters caused by photons that did not originate in neutral pion decays. However, the correlation between the respective energies and the opening angle of two photons due to a neutral pion decay can be checked for. In this thesis, methods for identifying single clusters are reviewed and only neutral pion events that resulted in a merged cluster were included in the further analysis. More details of the event selection will be given in Section 5.1.3.

In this thesis it is assumed that all clusters are caused by particles originating directly from the target. The neutral particles treated will not change their trajectories from interactions with the magnetic field in the detector and will thus strike the EMC detector in a direction pointing away from the target.

Cluster energy

An important basic parameter is the *cluster energy*, E_{cluster} , the total energy deposited in the digis belonging to a cluster:

$$E_{\text{cluster}} = \sum_d E_d, \quad (3.1)$$

where E_d is the energy deposited in digi d and the summation runs over all the digis in the cluster.

A fraction of the energy of the incoming particles will not be deposited in the crystals and will be lost⁷, but it is possible to try to compensate for this leakage. In the PandaRoot framework a ‘corrected cluster energy’ function is implemented that makes use of an empirical parametrization of the energy leakage for photons in the EMC as a function of $\ln E_{\text{cluster}}$ and θ [2, p. 143]. However, for this project just the sum over all the digis of a cluster was used, since exact values were not so important, but rather the separation power of the various methods that will be described in Chapter 4 and which for a large part do not rely on the energy correction.

⁷For instance, energy is lost in the gaps between crystals and from the detector energy threshold.

Cluster position

To find the exact position where the particle that caused a cluster had hit the crystals and thus to provide the center position of a cluster, a logarithmic energy-weighting average over all the digis in the cluster is used in PandaRoot, given by [2, p. 142]:

$$\mathbf{x}_{\text{cluster}} = \frac{\sum_d W_d \cdot \mathbf{x}_d}{\sum_d W_d}, \quad (3.2)$$

where \mathbf{x}_d is the position of digi d and the weights W_d are given by

$$W_d = \max \left\{ 0, A - B \cdot e^{-C \cdot E_{\text{cluster}}} + \ln \left(\frac{E_d}{E_{\text{cluster}}} \right) \right\}.$$

The default values of the parameters A , B and C in PandaRoot are given by $A = 3.6$, $B = 1.594$ and $C = 2.543 \text{ GeV}^{-1}$. Because only digis with non-zero weights contribute to the cluster position, the offset these parameters give has the effect of changing the minimal fraction of the cluster energy that a digi must have before it is used in the determination of the cluster position.

The logarithmic weighting takes into account that the radial energy distribution of an electromagnetic shower decreases mainly exponentially, assuming that the cluster was caused by a single particle. If this logarithmic weight results in non-zero values for less than two digis, a linear energy-weighted average of the digi positions is taken instead. For this project it was assumed that this method of determining the position of a cluster with the default parameter values gives good results, without investigating this in detail.

3.2.3 Bumps

Each cluster is finally split into *bumps*: each bump represents the digis belonging to a local maximum in the energy deposition of a cluster (i.e. a single incoming particle). As each cluster has at least one local maximum, the number of bumps is larger than or equal to the number of clusters.

Splitting clusters into bumps is a two-step process: first the digis that form the local maxima of a cluster are marked, and then all digis of the cluster are divided between the found maxima [2, p. 141–142]. To determine whether digi d becomes a local maximum, the following criteria are used in PandaRoot⁸:

- it has an energy E_d of at least 20 MeV;
- it has no neighboring digis with a higher energy;
- $E_{\text{max},n}/E_d < 0.5 \cdot (n - 2.5)$, where n is the number of neighboring digis with an energy of at least 2 MeV, and $E_{\text{max},n}$ is the energy of the most energetic neighbor.

After the local maxima of a cluster have been identified, each becomes a bump and the digis of the cluster are ‘shared’ between these, taking into account the expected exponential shower shape of each bump. This is done using an iterative algorithm which assigns a weight to each digi–bump combination, so

⁸The default values in PandaRoot are given for the energy cuts, etc.

that for each bump b , $E_{\text{bump}b} = \sum_d w_{bd} E_d$, where the summation runs over all the digis within the cluster. For each bump, the weights w_{bd} are calculated as

$$w_{bd} = \frac{E_d \cdot e^{-2.5 \cdot r_{bd}/R_m}}{\sum_i E_i \cdot e^{-2.5 \cdot r_{i,d}/R_m}},$$

where r_{id} is the distance between the d th digi and the center of the i th bump in the cluster, and R_m is the Molière radius of the crystal material (see Section 2.2.3). The summation with index i runs over all bumps of the cluster⁹. Note that these weights ensure that $\sum_b w_{bd} = 1$.

The calculation of the weights is iterated until convergence, where the center positions of the bumps at each iteration after the first are determined from the weights of the previous iteration, plugged into expression (3.2). Note that any bump can also be interpreted as a cluster, because a bump is still a set of neighboring digis, only with a weighting factor applied to the energy of each digi.

The bump-splitting procedure is the principal method handling multi-photon clusters in PandaRoot. Using such a bump-splitting algorithm has the important advantage that, in principal, there is no need to differentiate between photons in separate clusters and photons in merged clusters, as each photon should produce a single bump. This transparently removes the significance of the somewhat artificial way in which digis are grouped into clusters.

The information of the digis, clusters and bumps will be used in the further analysis, as described in Chapters 4 and 5.

3.3 Examples

In this section some examples of simulation results will be shown. The simulation parameters that were used to generate the data for this project will be discussed in detail in Chapter 5. The examples in this section are merely meant to illustrate some aspects of PandaRoot and the simulated $\bar{\text{PANDA}}$ detector itself.

3.3.1 Clusters

As the most important goal of this project is to provide a way to differentiate between one-photon and two-photon clusters, an instance of both types of clusters will be shown in this section, with a comparison between the full Monte Carlo information and the simulated response of the crystal detectors.

One-photon event

Figure 3.1 shows the energy response of the EMC for a photon event with $p = 6 \text{ GeV}/c$, $\theta = 55^\circ$ and $\phi = 69^\circ$. Both the energy deposition as given by the Monte Carlo information as the simulated response of the individual crystal detectors is plotted.

The approximately exponential decay in radial direction of the deposited energy can be seen in the Monte Carlo information. The actual detector response

⁹Note that the summation given in [2, p. 142] is incorrectly described as running over all digis in the cluster instead of over the bumps.

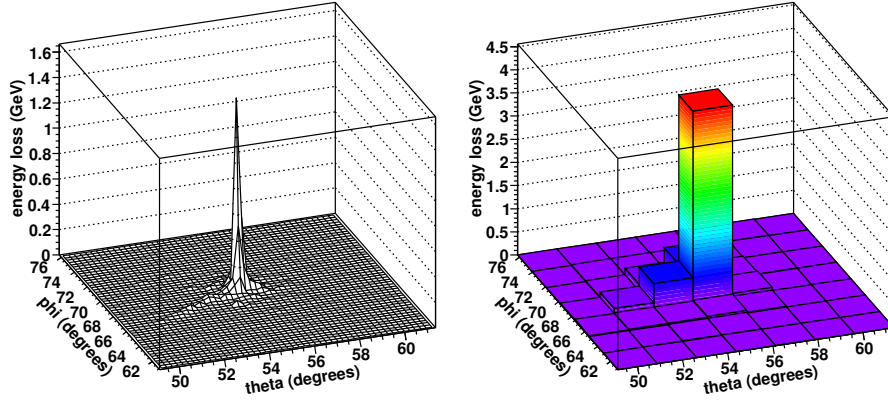


Figure 3.1 – The energy distribution as a function of θ and ϕ for a single simulated photon hitting the barrel EMC. (**Left panel**) actual energy distribution extracted from the Monte Carlo information and (**right panel**) simulated detector response per crystal.

gives a much coarser image due to the size of the crystals. Most of the photon energy was deposited in a single crystal, with the surrounding crystals only receiving a small part of the incident energy.

Two-photon event

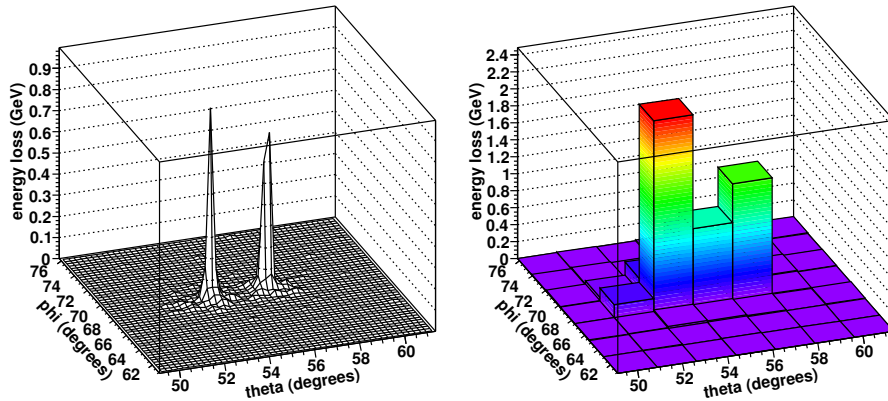


Figure 3.2 – The energy distribution as a function of θ and ϕ for the two photons of a simulated neutral pion event hitting the barrel EMC. (**Left panel**) actual energy distribution extracted from the Monte Carlo information and (**right panel**) simulated detector response per crystal.

Figure 3.2 shows the energy response of the EMC for a neutral pion event with $p = 6 \text{ GeV}/c$, $\theta = 55^\circ$ and $\phi = 69^\circ$. Again both the Monte Carlo information and the simulated detector response are plotted.

The electromagnetic showers induced by the two photons are clearly visible in the plot obtained from the Monte Carlo information. However, in the detector

response, both photons have formed a single merged cluster, as there are no crystals separating the two without any energy deposited in them. In this example, the two maxima of the cluster can still be easily identified.

3.3.2 Neutral pion opening angle

As described in Section 2.3.1, the primary decay channel of the neutral pion is into two photons, where the relative energies of the photons are related to the opening angle between their emission directions. Figure 3.3 depicts the simulated distribution of the opening angles of neutral pions with momenta between 0 and 15 GeV/c.

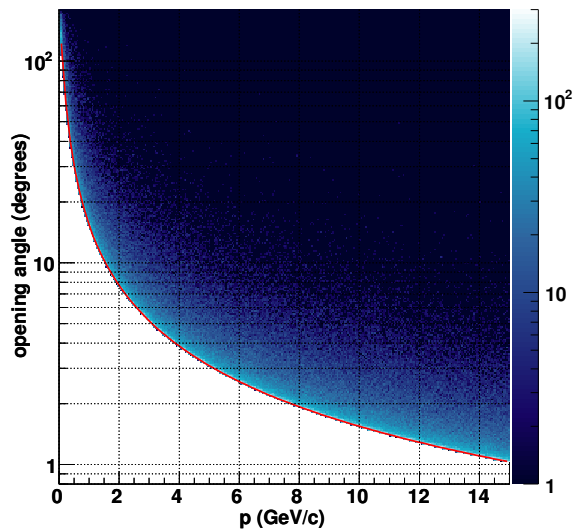


Figure 3.3 – The distribution of the opening angle of the decays of $4 \cdot 10^5$ simulated neutral pion events as a function of momentum. Note the logarithmic coloring. The red line is the theoretical minimum opening angle and it can be seen that most pion events have an opening angle close to this minimum, resulting in merged clusters for high-momentum events. This plot can be compared to Figure 2.5.

3.3.3 Energy loss

As described in section 2.2, photons (either single photons or those from neutral pion decays) will in general deposit their full energy in the crystals of the EMC. Their energy loss pc/E_{cluster} (see Section 4.1.1) should therefore be close to unity. Neutrons, on the other hand, generally do not deposit their full energy in the crystals. In fact, about a third of all simulated neutrons did not interact with the EMC.

To illustrate the difference between the electromagnetic showers formed by photons and the showers formed by neutrons, a spectrum of the energy loss of simulated particles is plotted in Figure 3.4. The photon events form a sharp

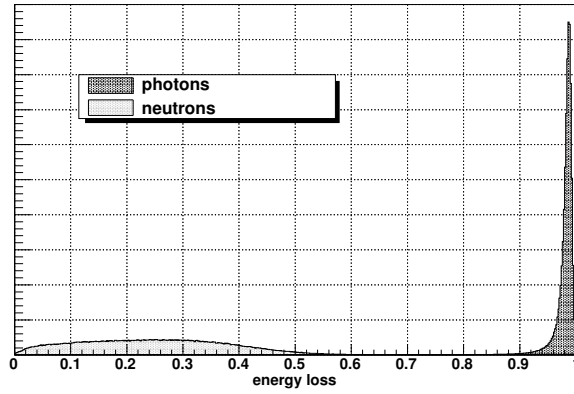


Figure 3.4 – Histogram of the fraction of energy lost, $E_{\text{cluster}}/(pc)$, for $2 \cdot 10^5$ neutron and photon events with momenta between 0 and 15 GeV/c.

peak close to 1, while the energy loss of the neutrons is distributed more widely, with a mean of about a quarter of their kinetic energy deposited in the EMC.

Chapter 4

Cluster Parameters

There are a lot of different parameters imaginable when it comes to capturing the shape of a cluster in the EMC. As described in Section 3.2.3, PandaRoot contains the bump-splitting algorithm to handle multi-photon clusters. The information of these bumps can be used in the identification of clusters.

In Chapter 6 the efficiency of the bump-splitting algorithm will be investigated and shown that it does not provide perfect results. For this reason it could be interesting to turn to parameters that take all the digis of a cluster into account for the identification, also known as *shower shape parameters*. In the PandaRoot framework a considerable number of cluster parameters are already implemented. In this chapter a selection of parameters that could be useful in the classification process of clusters is presented. All of these parameters were investigated during the course of this project for their ability to differentiate between the clusters caused by the different types of neutral particles. The corresponding results will be discussed in Chapter 6.

In the case that the bump-splitting method works well, it turns out that shower shape parameters also provide a powerful identification. In the case that the bump-splitting fails, due to maxima falling in adjacent crystals, using (a combination of) shower shape parameters might still provide a method for identification. The separation efficiency achievable using cluster parameters should therefore correspond to an upper limit of the separation efficiency that is achievable. It might turn out that this is more than will be required during the actual experiment and that the separation power of the bump-splitting algorithm, possibly optimized in some way, is sufficient. However, even in this case using shower shape parameters may have the advantage of requiring less calculation-power than the iterative bump-splitting algorithm.

In this thesis the identification of *clusters* is treated: these groupings of crystal responses are based on the detector geometry as described in Section 3.2.2. Clusters are convenient to use because they will generally be formed from the showers of a single particle or a small number of related particles. However, it is important to note that most of the parameters described in this chapter can be applied to any set of digis and are not necessarily limited to clusters.

4.1 General parameters

In Section 3.2.2, the cluster energy E_{cluster} and cluster position $\mathbf{x}_{\text{cluster}}$ were introduced. These do not provide any separation power on their own, but they can be used in combination with other parameters and are also needed as input for the calculation of several parameters.

4.1.1 Energy loss

As described in Section 2.2 and shown in Section 3.3.3, an important difference between clusters caused by neutrons and clusters caused by photons, is what fraction of its energy the particle deposits in the EMC crystals. Photons are absorbed entirely, $E_{\text{cluster}} \approx E_{\gamma}$, while heavier particles like neutrons only lose part of their kinetic energy and are not stopped completely by the EMC. The energy loss should thus provide a measure to distinguish between neutrons and photons.

The fraction of energy a particle lost in the EMC can be approximated¹⁰ as $E_{\text{cluster}}/(pc)$ and this parameter has been shown to be very important in the identification of charged particles [2, p. 144–146] [8]. However, the momentum p cannot be independently determined for neutral particles and thus it is not possible to use this parameter for the identification of neutral particles. It is therefore necessary to rely on the analysis of the cluster shape.

4.2 Bump parameters

The parameters in this section make use of the bumps in a cluster found by the bump-splitting algorithm described in Section 3.2.3.

4.2.1 Bump multiplicity

An obvious candidate for a parameter is the bump multiplicity of a cluster. Clusters that are caused by a neutral pion decaying into two photons should have two local maxima, while the clusters originating from a single photon should have only a single maximum. This, however, is a simplification from reality, because irregularities in showers can produce additional (small) local maxima.

4.2.2 Invariant mass reconstruction

As was shown by equation (2.2), in the case neutral pions decay into two photons, the energies of both photons and the angle between them are related via the invariant mass of the pion. This means that a possible criterion to distinguish the different cluster types would be to check whether there are two bumps present with energies and an opening angle consistent with that of a neutral pion decay:

$$mc^2 = \sqrt{2E_{\gamma_1}E_{\gamma_2}(1 - \cos\theta)}. \quad (4.1)$$

¹⁰Note that $E_{\text{kinetic}} = \sqrt{p^2c^2 + m^2c^4} - mc^2 < pc$ for particles that have a non-zero mass.

If the mass calculated in this way equals that of a neutral pion, i.e. $m \approx m_{\pi^0}$, then the cluster was likely due to the decay of a high-momentum pion. For other particle types, only a single main bump would be expected, and any secondary bumps from irregularities in the cluster shape should not be consistent with $m \approx m_{\pi^0}$ in equation (4.1). This parameter can thus be used to distinguish pion clusters from other types.

A downside of using the invariant mass reconstruction is the need to find the bumps within the cluster. Especially for very high-momentum pions it is difficult to identify the two bumps, since the maxima of the photons typically lie within one or two crystals from each other. The bump-finding algorithm implemented in PandaRoot, described in Section 3.2.3, is the limiting factor on the effectiveness of this parameter in identifying particles. The invariant mass reconstruction technique is also described in [9, p. 25–39], but using a different method of finding bumps than the one implemented in PandaRoot.

4.3 Shower shape parameters

The invariant mass reconstruction treated in the previous section is the physical way of checking whether two photons could have been due to a neutral pion decay. The invariant mass can be calculated in all cases and in principle it makes no difference whether the two photons ended up in the same cluster or not. However, the difficulty of correctly identifying the bumps within a cluster at very high momentum makes it interesting to look at other parameters that take the shape of the entire cluster into account.

In this section, various shower shape parameters will be presented that could be useful in the identification of particles. They will be tested for their performance in distinguishing one-photon clusters from two-photon clusters, based on the energy distribution represented by the digis of a cluster. Most of the parameters are already implemented in the PandaRoot framework in some form. In many cases they were taken over from the code of other experiments where these proved to be useful.

4.3.1 Cluster energy fractions

A promising parameter for identification is taking the fraction of the total cluster energy E_{cluster} in the n most energetic digis:

$$f_{\text{max},n} = \frac{\sum_{i=1}^n E_{\text{max},i}}{E_{\text{cluster}}}, \quad (4.2)$$

where $E_{\text{max},i}$ is the energy of the digi with the i -th highest energy within the cluster. Because the number of maxima differs between one-photon and two-photon clusters, this parameter will likely show a difference when n is properly chosen. This parameter is also discussed in [9, p. 48–53].

Alternatively, and already implemented in PandaRoot, one can take the ratio of different groups of digis centered on the digi containing the cluster position, to provide a measure of the radial decay of the shower. These sets of digis are square blocks of 1×1 , 3×3 and 5×5 digis centered on the most energetic digi of the cluster, giving E_{\square_1} , E_{\square_9} and $E_{\square_{25}}$. The ratios of these energies can provide

some information about the radial shape of the cluster. Also, the fraction of the total cluster energy in any of these blocks can be interesting. Therefore, define

$$f_{\square 1} = \frac{E_{\square 1}}{E_{\text{cluster}}} = f_{\max, 1}, \quad f_{\square 9} = \frac{E_{\square 9}}{E_{\text{cluster}}} \quad \text{and} \quad f_{\square 25} = \frac{E_{\square 25}}{E_{\text{cluster}}}. \quad (4.3)$$

4.3.2 Cluster mass

Also implemented in PandaRoot is a so-called ‘cluster mass’, defined as¹¹:

$$m_{\text{cluster}}c^2 = \sqrt{E_{\text{cluster}}^2 - \left\| \sum_d E_d \hat{\mathbf{x}}_d \right\|^2}, \quad (4.4)$$

where the summation d runs over all digis in the cluster. Note that this parameter does not directly correspond to any physical mass, but could nonetheless help in the identification of particles. Because the energy in two-photon clusters is spread out more than the energy in one-photon clusters, the cluster mass of two-photon clusters will likely be higher.

4.3.3 Cluster moments

An important way of assessing the shape of an electromagnetic shower is to make use of *cluster moments*, which are discussed in [9, p. 40–47] and [10]. A cluster moment of degree n of some variable ξ is the energy-weighted average taken over all the crystals d in a cluster:

$$\langle \xi^n \rangle = \frac{1}{E_{\text{cluster}}} \sum_d E_d \xi_d^n. \quad (4.5)$$

Promising variables to capture the shower shape of a cluster are the first and second moments of θ and ϕ , as well as the lateral position $r = \|\mathbf{x}'\| = \|\mathbf{x} - \mathbf{x}_{\text{cluster}}\|$. Note that in [10], \mathbf{x}' is split into a lateral and longitudinal part, based on the shower axis vector. This axis is determined by a principal value analysis of the energy weighted spatial correlation with respect to the cluster center, but since the PANDA EMC only has a single layer of crystals, this cannot be done and no longitudinal information can be extracted. Taking the vector from the target as the shower axis and then taking only the perpendicular part of \mathbf{x}' as the lateral position can be done. Something similar will be done in the calculation of the Zernike moments in the next section, but the difference with just using \mathbf{x}' will be minimal. The first and second cluster moments of several variables, including those mentioned here, are available in PandaRoot.

In [10], a normalization scheme for the lateral moment is proposed by defining

$$\text{lat} = \frac{\text{lat}_2}{\text{lat}_2 + \text{lat}_{\max}}, \quad (4.6)$$

where lat_2 is $\langle r^2 \rangle$ with $r_d = 0$ for the two most energetic crystals, and lat_{\max} is $\langle r^2 \rangle$ with $r_d = 5$ cm for the two most energetic crystals and $r_d = 0$ for all other crystals. This will normalize the lateral moment to the interval $[0, 1]$. The same method can also be applied to moments of a different order or variable.

¹¹The notation $\hat{\mathbf{x}}$ is used to denote the unit vector in the direction of vector \mathbf{x} .

4.3.4 Zernike moments

The Zernike polynomials are a set of orthogonal complex polynomials defined on the unit disk named after Fritz Zernike¹² that can be used to describe the shape of an optical lens. Although their form originates from the study of circular wavefronts, they can also be used to calculate moments based on the energy distribution within a cluster. In PandaRoot, a function is implemented to calculate the Zernike moments of a cluster.

The complex Zernike polynomial with subscripts m , $n \in \mathbb{Z}$ with $n \geq m \geq 0$ can be defined as [12]:

$$U_n^m(\rho, \varphi) = R_n^m(\rho)(\cos(m\varphi) - i \sin(m\varphi)),$$

where the radial part is given by

$$R_n^m(\rho) = \begin{cases} \frac{1}{2}^{(n-m)} \sum_{k=0}^{\frac{1}{2}(n-m)} \frac{(-1)^k (n-k)!}{k! (\frac{1}{2}(n+m)-k)! (\frac{1}{2}(n-m)-k)!} \rho^{n-2k} & \text{for } n-m \text{ even;} \\ 0 & \text{for } n-m \text{ odd.} \end{cases}$$

The Zernike polynomials are defined on the two-dimensional polar coordinate system (ρ, φ) for $0 \leq \rho \leq 1$. To make use of Zernike moments, a transformation from the three-dimensional position of the digis of a cluster into this coordinate system is needed. Since the EMC crystals are laid out in an approximately spherical single layer around the target, a straightforward way to do this is to construct a two-dimensional coordinate system orthogonal to the vector to the origin (see Figure 4.1), by defining

$$(\rho_d, \varphi_d) = \left(\frac{1}{\rho_0} \|\mathbf{r}_d\|, \sin^{-1} \left(\hat{\Phi} \times \hat{\mathbf{r}}_d \cdot \hat{\mathbf{x}}_{\text{cluster}} \right) \right),$$

with $\mathbf{r}_d \equiv \mathbf{x}_d - (\mathbf{x}_d \cdot \hat{\mathbf{x}}_{\text{cluster}}) \hat{\mathbf{x}}_{\text{cluster}}$, $\mathbf{x}'_d \equiv \mathbf{x}_d - \mathbf{x}_{\text{cluster}}$ and $\Phi \equiv \mathbf{x}_{\text{cluster}} \times \hat{\mathbf{v}}$.

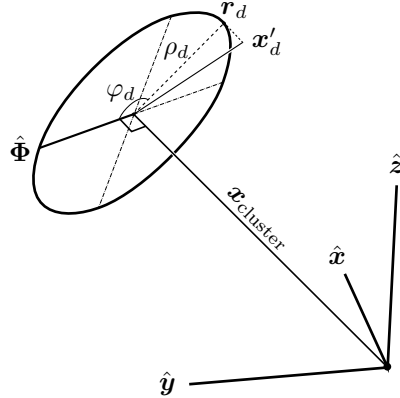


Figure 4.1 – Construction of the local coordinate system.

¹²Fritz Zernike, 1888–1966.

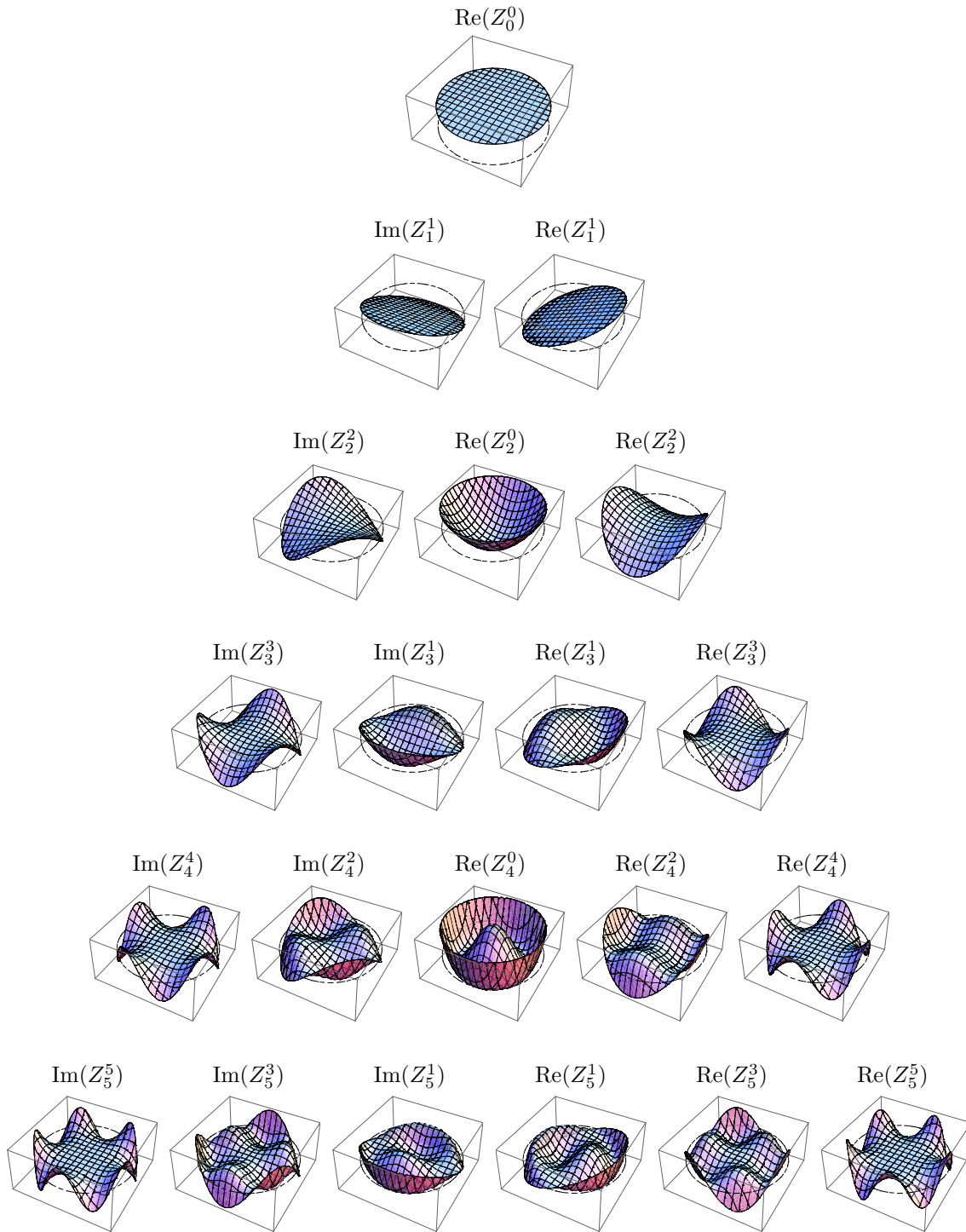


Figure 4.2 – Plots of the real and imaginary components of the Zernike polynomials Z_n^m with $0 \leq n \leq 5$. Polynomials with $m = 0$ are real-valued.

Here the vector Φ determines the direction of $\varphi = 0$, and \mathbf{v} can be chosen as any vector non-parallel to $\mathbf{x}_{\text{cluster}}$; for instance, it can be taken as the z -axis, $\mathbf{v} \equiv \hat{\mathbf{z}}$, because there are no EMC crystals positioned on the z -axis. Note that a normalization constant ρ_0 is used to bring the position of all (or most) digis of a cluster to within $0 \leq \rho_d \leq 1$.

The Zernike moment with subscripts m, n of a cluster can be defined as:

$$Z_n^m = \frac{1}{E_{\text{cluster}}} \left\| \sum_d E_d R_n^m(\rho_d) (\cos(m\varphi_d) - i \sin(m\varphi_d)) \right\|. \quad (4.7)$$

By taking the norm of the complex result, this measure actually becomes independent of the direction of the φ -axis in the two-dimensional plane. When the local coordinate system is constructed as described before, the φ -axis has no special significance, and its orientation with respect to the shape of a particular cluster is essentially random. However, if the φ -axis would in each case be aligned to, for example, the major axis of a cluster as described in Section 4.3.5, then the angle of the complex Zernike moment could yield additional information. This was not investigated in depth during this project.

4.3.5 Eccentricity

The energy distribution of a cluster formed by a single photon hitting the EMC in a direction directly away from the target should be on average radially symmetric. Clusters formed by the two photons of a pion decay should clearly be less symmetric. Parameters that assess how radially symmetric a cluster is, could thus be interesting for classification purposes.

Major and minor axes

The shape of a cluster is the primary difference between a two-photon cluster and a cluster caused by a single photon or neutron. One way to try to capture this information, is to measure the elongation of a cluster, by assuming it has a shape that is approximately elliptical. The first step is to find the major and minor axes of a cluster, which are assumed to be orthogonal. In this project, these axes were found by applying a linear least-squares fitting to the digi positions in a cluster taken within a local two-dimensional coordinate system, where the positions of the digis are weighted by their energy. Although the PandaRoot framework already contains functions to obtain the parameters relating to the major and minor axes of a cluster, the method described in this section is somewhat different from the one used in PandaRoot.

In a linear least-squares fitting, the squares of the vertical offsets from a line (or any other function) are minimized to find the line that best fits the data. The results of this method are not independent of the orientation of the local coordinate system, as it minimizes the offsets in y -direction for given values of x . Since in the local coordinate system (ρ, φ) defined earlier the orientation of clusters with respect to the φ -axis is arbitrary, it is better to use the least-squares method that minimizes the squares of the perpendicular offsets, which are independent of the orientation of the coordinate system (see Figure 4.3) [11].

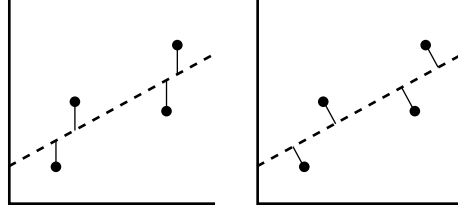


Figure 4.3 – This figure illustrates the different offsets that are minimized in the case of a linear least-squares fitting with vertical offsets (**left panel**) and perpendicular offsets (**right panel**) [11, Fig.].

The best-fit coefficients¹³ for the line $a + bx$ can be calculated from the digit positions in a local two-coordinate system (x_d, y_d) as follows [11]:

$$b_{\pm} = -B \pm \sqrt{B^2 + 1},$$

where B is given by

$$B = \frac{1}{2} \frac{\sum_d E_d (y_d^2 - \bar{y}^2) - \sum_d E_d (x_d^2 - \bar{x}^2)}{\sum_d E_d \bar{x} \bar{y} - \sum_d E_d x_d y_d}.$$

Using the coordinate system (ρ, φ) described before, x_d and y_d can be defined as $x_d = \rho_d \cos \varphi_d$ and $y_d = \rho_d \sin \varphi_d$.

Note that the equation above gives two orthogonal solutions b_+ and b_- for each cluster, corresponding to the major and minor axes. The second moment of the distance from both axes was calculated to decide which solution was the major axis. For instance, taking the b_+ solution and calculating the parallel and orthogonal moments as

$$\langle r_{\parallel}^2 \rangle = \frac{1}{E_{\text{cluster}}} \sum_d E_d (\mathbf{r}_d \cdot \hat{\mathbf{a}})^2 \quad \text{and} \quad \langle r_{\perp}^2 \rangle = \frac{1}{E_{\text{cluster}}} \sum_d E_d \|\mathbf{r}_d - (\mathbf{r}_d \cdot \hat{\mathbf{a}}) \hat{\mathbf{r}}_d\|^2,$$

where $\mathbf{a} \equiv (\cos \alpha, \sin \alpha)$ with $\alpha \equiv \tan^{-1}(b_+)$.

If $\langle r_{\parallel}^2 \rangle > \langle r_{\perp}^2 \rangle$, then b_+ corresponds to the major axis of the cluster, otherwise b_- corresponds to the major axis, i.e., the average squared distance parallel to the major axis should be larger than the average squared distance orthogonal to it. Although there might be other ways of determining the minor and major axes, this method of using the second moments gives generally good results.

At this point, the moments $\langle r_{\text{major}}^2 \rangle$ and $\langle r_{\text{minor}}^2 \rangle$ can be defined as, respectively, the second moment of the distance from the major axis and the second moment of the distance from the minor axis:

$$\langle r_{\text{major}}^2 \rangle = \min\{\langle r_{\parallel}^2 \rangle, \langle r_{\perp}^2 \rangle\} \quad \text{and} \quad \langle r_{\text{minor}}^2 \rangle = \max\{\langle r_{\parallel}^2 \rangle, \langle r_{\perp}^2 \rangle\}. \quad (4.8)$$

Assuming that the cluster has a regular, approximately elliptical shape, the ratio between these moments describes this shape, whether the cluster is circular or more elongated. Interpreting these moments as the major and minor axes of

¹³Coefficient a is not used here; it is assumed that the major axis passes approximately through the calculated cluster center position x_{cluster} .

an ellipse, it is possible to define a parameter analogous to the eccentricity of an ellipse as:

$$\epsilon_{\text{cluster}} = \sqrt{1 - \frac{\langle r_{\text{major}}^2 \rangle}{\langle r_{\text{minor}}^2 \rangle}}. \quad (4.9)$$

Eccentricity integral

Another parameter based on the eccentricity of clusters that was investigated during this project is the ‘eccentricity integral’, defined as:

$$\mathfrak{I}_{\text{cluster}} = \sum_d \rho_d^2 \left| E_d - \tilde{E}(\rho_d) \right|, \quad (4.10)$$

where $\tilde{E}(\rho)$ is the ‘average energy per digi at a distance of ρ from the cluster center’.

The eccentricity integral tries to capture how radially symmetric a cluster is by not only taking the averaged radial distribution of energy into account, but also the φ -dependence of the distribution. This is done by summing the absolute value of the difference between the energy deposited in each digi of a cluster and the average energy deposition at that radial distance from the cluster center. In addition, this energy difference is weighted by the square of the radial distance of the digi. For clusters with an energy distribution that is perfectly radially symmetric, this parameter would give a value of zero. Any asymmetry will result in a larger value.

There are multiple ways of defining $\tilde{E}(\rho)$. Because the number of digis is limited, there is no continuous energy distribution and $\tilde{E}(\rho)$ has to be estimated in some way. For this project, the simple method of making a histogram containing the energy as a function of the radial distance was used. To obtain $\tilde{E}(\rho)$, the two-dimensional plane was first split into a set of annuli with equal widths $\Delta\rho$. For each annulus, the average energy deposition per digi was calculated and used as \tilde{E} for that part of the plane. Note that there are smoother density estimation algorithms, e.g. the Parzen window method, that might give better results, but this was not investigated.

The results of the classification analysis based on the parameters treated in this chapter will be given in Chapter 6. First, a description of the way the data for this project was generated and how it was analyzed will be given in Chapter 5.

Chapter 5

Analysis

In this chapter, the simulation process and the techniques that were used in the data analysis for this project are described.

5.1 Data generation

While the computer simulation for the $\bar{\text{P}}\text{ANDA}$ experiment itself was already discussed in Chapter 3, this section deals with the simulation parameters that were used to obtain the data for this project.

5.1.1 EMC geometry considerations

As described before, the information that the electromagnetic calorimeter of the $\bar{\text{P}}\text{ANDA}$ detector provides is the deposited energy for each crystal. Because during the experiment most neutral pions will decay close to the target position, the size of the EMC crystals as seen from the target determines the angle at which the merged clusters described in Section 3.2.2 will start to appear.

The differentiation between one-photon and two-photon clusters becomes increasingly difficult when the maxima of the two showers lie closer together in terms of crystals and becomes essentially impossible if both photons hit the same crystal. The ‘granularity’ of the detector as seen from the target thus sets the lower limit for the opening angle between two photons that can be resolved. Since the opening angles allowed for neutral pion decays depend on the momentum of the pion, as discussed in Section 2.3.1, this places an upper limit on the momentum of neutral pions that can successfully be identified.

The design of the $\bar{\text{P}}\text{ANDA}$ detector as a whole and specifically the target spectrometer EMC takes into account that particles will be boosted in forward direction due to the beam momentum. The granularity is not the same in all directions from the target position and the highest granularity can be found in the forward direction. Even though the crystals of the forward end-cap have a frontal area slightly larger than that of the crystals of the barrel part, they are placed at a larger distance from the target position and consequently cover a smaller solid angle.

In Figure 5.1, an illustration of the granularity of the forward spectrometer EMC is given by plotting the projection of the front faces of all crystals of the

EMC as a function of θ and ϕ . The more crystals present per unit solid angle, the better the detector will be able to resolve small opening angles. Clearly the granularity of the EMC is higher in forward directions, with the forward end-cap having the most crystals per unit solid angle. The backward end-cap and the part of the barrel that is closest to the target position (around $\theta = 90^\circ$) have the worst granularity.

To provide a (qualitative) measure of the angular resolution of the EMC, the reciprocal of the average solid angle that the crystals cover as a function of θ is plotted in Figure 5.2. The breaks in the curve correspond to the gaps between the barrel module and the two end-caps.

An interesting aspect of the design of the EMC is that for the forward end-cap, the resolution improves somewhat with increasing θ . This is caused by the geometry of the end-cap, where all crystals have the same size, but the crystals at the edge of the end-cap are placed further from the target position than the crystals at the center. For the barrel part and the backward end-cap, the same holds: the main factor determining the angular resolution is the distance of the crystals from the target position.

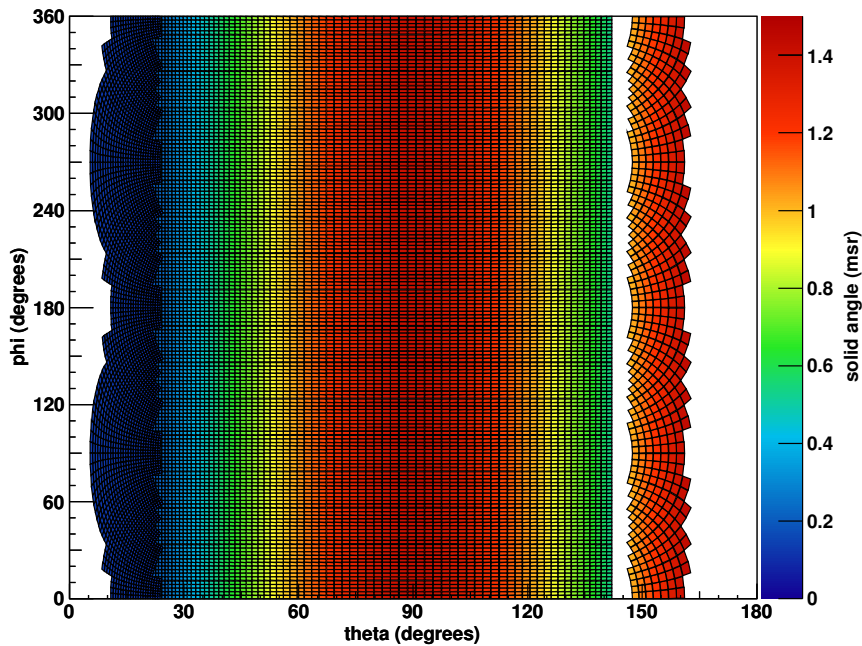


Figure 5.1 – An illustration of the granularity of the EMC as seen from the target position, as a function of θ and ϕ . The projections of the front faces of all crystals are plotted, colored according to the solid angle they cover. A smaller solid angle corresponds to a better angular resolution. The left part of the plot corresponds to the forward end-cap, the central crystals form the barrel and the backward end-cap is on the right hand side of the plot. Note the holes for the beam pipe at $\phi = 0^\circ$ and $\phi = 180^\circ$, and the gap in the acceptance between the barrel and the backward end-cap modules. The figure depicts the most recent design for the forward end-cap geometry, which was used in the simulations for this project.

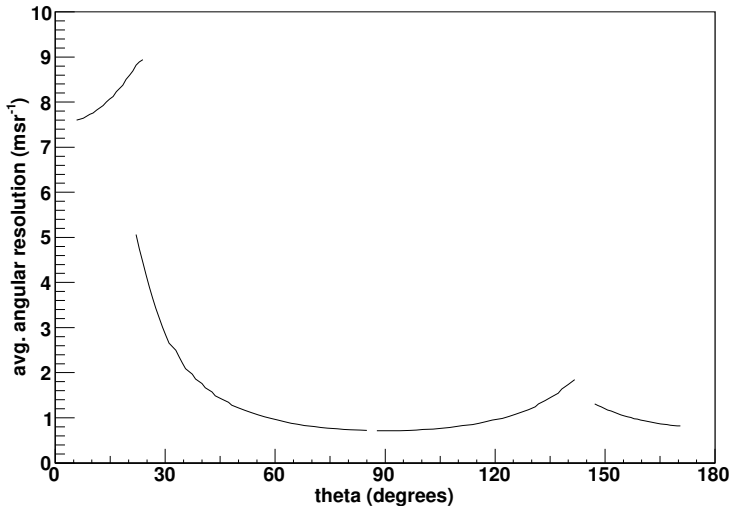


Figure 5.2 – Reciprocal of the average solid angle that the crystals of the EMC cover, as a function of θ .

As shown, the granularity of the EMC depends strongly on θ . This is an intentional part of the design, as the momentum distribution of particles formed during the experiment will also depend on θ . An example of the momentum spectra for the different modules of the EMC for a cocktail of simulated events at the maximum beam momentum of 15 GeV/c are given in [2, Fig. 3.4, p. 35]. Here it is shown that the maximum momentum of neutral pions striking the backward end-cap of the EMC is < 1 GeV/c, for the barrel part it is ≈ 7 GeV/c and for the forward end-cap the maximum momentum increases up to ≈ 14 GeV/c. The average neutral pion momenta are < 1 GeV/c for the backward end-cap, ≈ 2 GeV/c for the barrel part and ≈ 5 GeV/c for the forward end-cap.

Because the granularity of the EMC determines the smallest opening angle that can be resolved, the attainable efficiency of the separation between one-photon and two-photon clusters will also vary with θ . Assuming that the momentum distribution of particles formed during the $\overline{\text{PANDA}}$ experiment will mainly decrease with increasing θ , two regions where the reconstruction efficiency of the EMC might be limited are the inner edge of the forward end-cap (at θ between 5° and 10°) and the part of the barrel closest to the target position (around $\theta = 90^\circ$). However, more detailed information about the expected momentum distributions as a function of θ would be needed to test this.

To investigate the effects of the granularity on the separation efficiency, two separate data sets were generated for this project:

- a data set for the *forward end-cap* with $\theta = 14^\circ$, representing the part of the EMC with the highest granularity, where the opening angle between two crystals is about 0.8° ;
- and a data set for the *barrel* with $\theta \in [80^\circ, 100^\circ]$, representing the part of the EMC with the worst granularity, where the opening angle between two crystals is about 2° .

The former data set was generated at a scattering angle about halfway down the forward end-cap to prevent the energy of particles from getting lost in the gap for the beam pipe and thereby negatively influencing the results.

For both data sets, particles were simulated with momenta uniformly distributed as $p \in [0, 15]$ GeV/ c . Although this is a very unrealistic momentum distribution, it is useful to investigate how the separation efficiency depends on the momentum of incoming particles. Note that the chosen momentum spectrum will influence the absolute separation efficiencies found. However, it is expected that the relative separation powers of the parameters investigated in this project will be similar. Because the momentum dependence of the separation efficiencies was investigated, it should also be possible to fold in the proper momentum distributions afterward to obtain more realistic efficiency values.

5.1.2 Simulation parameters

The following list summarizes the chosen simulation parameters discussed in Chapter 3 and the preceding section.

- transport model: GEANT3;
- particles simulated: γ , π^0 , n;
- momentum: $p \in [0, 15]$ GeV/ c (distributed uniformly);
- originating vertex: $\mathbf{v} = (0, 0, 0)$ cm (target position);
- direction: forward end-cap data set $\theta = 14^\circ$, barrel data set $\theta \in [80^\circ, 100^\circ]$; $\phi \in [0^\circ, 360^\circ]$ (distributed uniformly);
- number of events: $2 \cdot 10^5$ events per particle class (after event selection);
- geometry: only the geometry of the EMC subdetector was used in the simulation;
- other simulation, digitization and reconstruction parameters were taken with their default values.

5.1.3 Event selection

This section describes which simulated events were used in the further analysis. For the event selection, the full Monte Carlo information from the simulation was used. The rationale of the selection was to analyze only events where identification using the parameters described in Chapter 4 would be useful. As these parameters operate on clusters, only neutral pion events where a single merged cluster was formed were used in the analysis.

All events where the simulated particles did not interact with the EMC in any way were discarded. For the photon and neutral pion events, only very few had to be discarded ($\ll 0.1\%$). Neutrons seemed to interact with the EMC only about two-thirds of the time. This conditions was implemented by discarding all events without any clusters.

Selection rule: only events where the simulated particle had some interaction with the EMC are accepted. With the default simulation parameters, this includes an energy threshold of 3 MeV.

Of the neutral pion events, only those for which the pion decayed via its primary decay channel into two photons were accepted. Additionally, all events for which the two photons did not form a single merged cluster were discarded, as their identification was not the topic of this project. This condition was tested by finding the crystals closest to the emission directions of the two photons, obtained from the Monte Carlo information, and checking whether these two crystals were both part of the same cluster.

Selection rule (neutral pion events): only events are accepted for which the neutral pion decayed via its primary decay channel and for which both photons formed a single merged cluster.

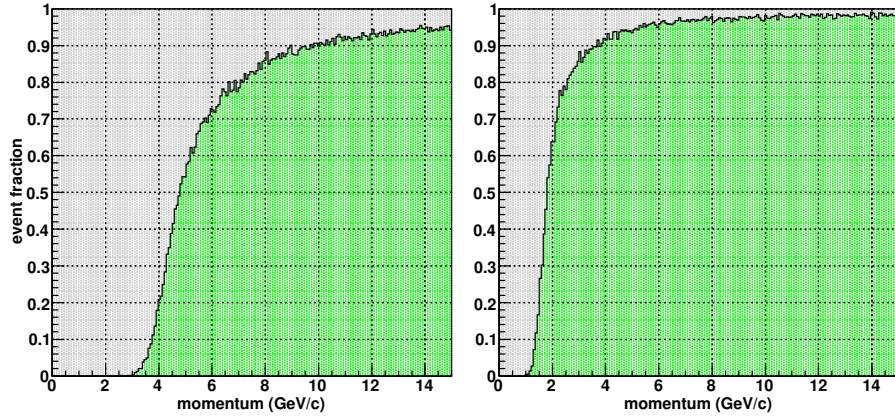


Figure 5.3 – The fraction of neutral pion events passing the event selection, as a function of momentum p , for the forward end-cap data set (**left**) and the barrel data set (**right**). By far the largest fraction of events was discarded due to the absence of merged clusters. The secondary Dalitz decay of the neutral pion accounted for the rejection of slightly more than one percent of the events, independent of momentum, in agreement with the branching ratio of this decay mode (see Section 2.3.1).

The events passing these selection rules were used in the further analysis. Figure 5.3 shows the fraction of neutral pion events used in the analysis as a function of momentum, for both data sets. As shown, there is a clear difference between the forward end-cap and barrel data sets in the fraction of clusters that are merged clusters at a certain momentum. For the forward end-cap data set, merged clusters start appearing around 3 GeV/ c and only above 12 GeV/ c the fraction becomes larger than 0.9. For the barrel data set, most neutral pion events result in merged cluster from momenta as low as 2 GeV/ c . At all momenta there are events for which the photons of a neutral pion decay formed two separate clusters, since large opening angles are always kinematically allowed, as can be seen from equation (2.3).

5.2 Analysis tools

In this section, the two methods that were used during this project to investigate the separation power of individual parameters or their combinations are described. To classify an event, a method must be found of assigning it to a certain particle class. In this project, the classification was based solely on the information from the EMC.

For the case of two particle classes (a binary classification problem), a simple algorithm to classify events is a *dichotomizer*: defining a certain threshold value of some parameter ξ , and classifying all events where the parameter value is above this threshold as the one class and the rest as the other. The parameter ξ could be one of the cluster parameters as discussed in Chapter 4, or a value calculated from a combination of them. To compare it with other parameters, a method of quantifying the classification efficiency of parameter ξ is needed. In this project, so-called *ROC curves* were used for this. These curves provide a method of visually presenting the separation efficiency that can be achieved in a binary classification problem using a threshold in a single parameter.

The ROC curve method, which will be described in more detail below, cannot be used for classification problems with more than two classes and only works on a single parameter. To classify all three classes of particles that were simulated in this project at the same time, and to investigate whether it is possible to improve the classification results by using multiple parameters, the *KNN algorithm* was used as a second method of analysis. The KNN algorithm is a multidimensional density estimator that estimates the probability distribution of all event classes considering the space spanned by a selection of parameters. This multivariate algorithm will be described in detail at the end of this section.

The results of applying both analysis methods to the data generated for this project will be given in Chapter 6.

5.2.1 Receiver Operating Characteristic curve

The *Receiver Operating Characteristic* (ROC) curve method allows to study the separation power that a single parameter provides. A ROC curve gives a visual representation of the separation efficiency that a binary classifier achieves. A single classifier results in a single point in a ROC plot. Classifiers that require an input value that can be continuously varied, like the dichotomizer mentioned before where the threshold value can be chosen freely, result in a ROC curve. How ROC curves can be generated and what information they convey will be described in this section, and an example will be given later.

A ROC curve is generated from a set of events of two classes. Such a data set of n events can be denoted by $\mathbb{D} = \{\xi_i, S_i^T\}_{i=1}^n$, where index i enumerates the events, $\xi_i \in \mathbb{R}$ is the parameter under consideration and $S_i^T \in \{\omega_1, \omega_2\}$ is the true class of event i , which will clearly be unknown during the actual experiment. Furthermore, define n_1 as the number of events of class ω_1 and n_2 as the number of events of class ω_2 , such that $n_1 + n_2 = n$.

A classification algorithm is used to determine a classification S_i from the data ξ_i . Ideally, it would hold for all events that $S_i = S_i^T$, but in general some events will be classified incorrectly. Note that some classification methods actually give a continuous classification result, i.e. a measure of the chance of event i belonging to class ω_1 between 0 and 1. Although the ROC curve

method as described here will assume a discrete classification method, it could be adapted to incorporate continuous classification results.

A simple discrete classification algorithm is the dichotomizer mentioned before: applying a threshold value in some parameter ξ , and classifying all events with ξ_i above this threshold as the one class and all events below this threshold as the other. Formally, this method applies the following classification rule for some value of $\xi_{\text{cut}} \in \mathbb{R}$:

$$S_i(\xi_{\text{cut}}) = \begin{cases} \omega_1 & \text{if } \xi_i < \xi_{\text{cut}}; \\ \omega_2 & \text{if } \xi_i > \xi_{\text{cut}}. \end{cases}$$

Note that this type of classification is not necessarily suited for every possible parameter. For this kind of classification to work well, the events of one class should have ξ_i values that are generally larger than those of the other class.

A ROC curve consists of plotting the fraction of events of class ω_1 classified *correctly* (i.e. events for which $S_i = S_i^T = \omega_1$) versus the number of events of class ω_2 classified *incorrectly* (i.e. events for which $S_i^T = \omega_2$, but $S_i = \omega_1$), for different values of ξ_{cut} . The ROC curve is thus parameterized by ξ_{cut} and each threshold value gives a single point $\mathbf{p}(\xi_{\text{cut}}) = (x(\xi_{\text{cut}}), y(\xi_{\text{cut}}))$ of the curve, given by:

$$\mathbf{p}(\xi_{\text{cut}}) = \left(\frac{1}{n_2} \sum_{i|S_i^T=\omega_2} [S_i(\xi_{\text{cut}}) \neq S_i^T], \frac{1}{n_1} \sum_{i|S_i^T=\omega_1} [S_i(\xi_{\text{cut}}) = S_i^T] \right),$$

where $[P]$ is the Iverson bracket:

$$[P] = \begin{cases} 1 & \text{if } P \text{ is true;} \\ 0 & \text{otherwise.} \end{cases}$$

Often the vertical axis is called the *true positive rate* (TP rate) and the horizontal axis is called the *false positive rate* (FP rate), where classifying events as class ω_1 and ω_2 are called classifying them as positive and negative, respectively. Note that for any finite data set, the ROC ‘curve’ will actually consist of a finite number of unconnected points, but these points can be regarded as approximating a continuous ROC curve. However, for parameters that take only discrete values, the ROC curve will always consist of a limited set of points and in these cases cannot really be regarded as a curve.

Interpretation

A sample parameter distribution and corresponding ROC curve is given in Figure 5.4, illustrating the concept. All points of the ROC curve lie within the square $[0, 1] \times [0, 1]$ and all ROC curves will include the points $(0, 0)$ and $(1, 1)$, as these represent classifying all events the same regardless of the parameter under consideration. Perfect classifiers are represented by the point $(0, 1)$. The diagonal from $(0, 0)$ to $(1, 1)$ is the ‘line of no-discrimination’: points on this line represent classifiers that perform as good as a completely random guess. Points further from the diagonal correspond to better classifiers.

The diagonal divides the ROC space into an area of good classification results above the diagonal and an area of ‘worse-than-random’ classification results below the diagonal. Note, however, that classifiers falling below the diagonal

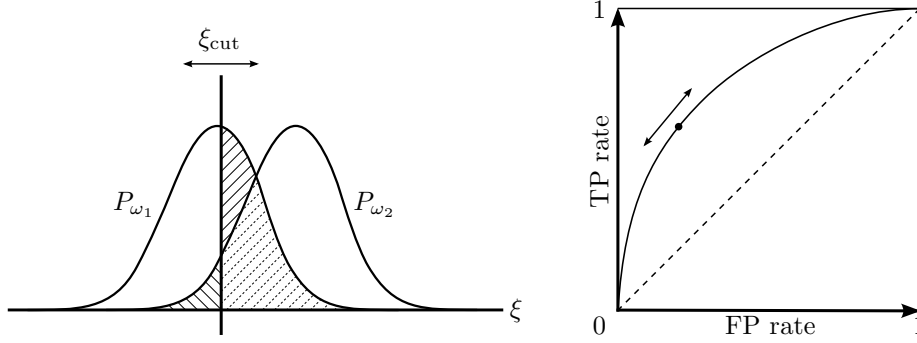


Figure 5.4 – Example of a ROC curve (**right panel**) generated from a fictitious parameter distribution (**left panel**). The misclassified events for a certain value of ξ_{cut} are indicated, as is the corresponding point on the ROC curve.

still provide useful separation information and by inverting all their classification decisions can be transformed to get points above the diagonal with equivalent separation power, i.e. mirroring in the point $(0.5, 0.5)$ or $(x, y) \rightarrow (1-x, 1-y)$. For this reason, the lower triangle is normally empty in ROC plots. The ROC curve obtained by switching the labels of the two classes, i.e. mirroring in the diagonal or $(x, y) \rightarrow (y, x)$ is also equivalent with respect to the separation power.

The strength of the ROC curve lies in the fact that it shows what classification possibilities there are using a single cut in the investigated parameter. What the best classification would be depends on which kind of classification errors are more important to prevent: it could be the case that classifying the events of one class correctly is more important than the classification of the events of the other class, resulting in a different choice of a best point in ROC space from what would be the case if both kinds of errors were equally important to minimize.

There are different ways of capturing the most important information from a ROC curve in a single number. In this project, the integral under the ROC curve was used as a measure of the total separation power of a parameter:

$$I = \int_0^1 y(x) dx. \quad (5.1)$$

This integral will be equal to 1 for a perfect classifier and 0.5 for a classifier that performs as bad as using a random guess.

5.2.2 k -Nearest Neighbor algorithm

The previously described ROC curves work on a single parameter. To investigate whether it is useful to combine multiple parameters in the classification process, a form of *multivariate analysis* (MVA) is needed. Furthermore, while ROC curves can be used to gauge the separation power of parameters for two event classes, this method cannot easily be extended to more classes.

There exist various algorithms to perform a multivariate analysis and several have already been used for the particle identification process in the $\overline{\text{PANDA}}$

project [2, p. 144–146] [8]. For this thesis, the *k-Nearest Neighbor* (KNN) algorithm was used. This algorithm approximates the probability density functions of all event classes in the space spanned by a chosen combination of parameters. To achieve this, a certain number of events are used as a ‘training set’ of which the true event classes need to be provided. Further events are then classified by evaluating the probability density functions at the points in parameter space of these events. Note that combining multiple parameters only helps if the parameters contain uncorrelated information.

While the KNN algorithm is not the most efficient algorithm regarding the computation power required, being something of a ‘brute force’ approach to the classification problem, it is easier to use and to understand than, for instance, neural networks. The KNN algorithm is discussed in [8, p. 24] and the Panda-Root framework contains a generic implementation of the algorithm that can be used for any classification problem.

Training

The KNN algorithm needs a set of events to approximate the probability density functions of the various event classes in parameter space. This is done by taking a part of the data set $\mathbb{D} = \{\boldsymbol{\xi}_i, S_i^{\text{T}}\}$ as the *training set* $\mathbb{T} \subset \mathbb{D}$, where the classes of events are known. This set is then used to estimate the probability density functions to allow the classification of the rest of the events, $\mathbb{D} \setminus \mathbb{T}$. Note that $\boldsymbol{\xi}_i$ is now an m -dimensional vector consisting of some combination of parameters and the events may belong to l different classes, $S_i^{\text{T}} \in \{\omega_1, \dots, \omega_l\}$. The training set should be taken to be representative of the entire data set.

Classification

To approximate the probability density functions of the different classes at some point $\boldsymbol{\xi}$ in parameter space, the KNN algorithm takes the k closest events in \mathbb{T} and evaluates the (known) classes of each of these events. To determine the closest events, a measure of distance is required. For this usually the Euclidean distance in \mathbb{R}^m is used:

$$d(\mathbf{p}, \mathbf{q}) = \sqrt{\sum_{i=1}^m (p_i - q_i)^2}.$$

Denoting the k closest events in parameter space using this measure of distance as $\{\boldsymbol{\xi}_{t_i}, S_{t_i}^{\text{T}}\}_{i=1}^k \subset \mathbb{T}$, the probability density function of a class ω_j can be approximated as

$$P(\omega_j|\boldsymbol{\xi}) = \frac{1}{k} \sum_{i=1}^k \delta(S_{t_i}^{\text{T}}, \omega_j),$$

where $\delta(i, j)$ is the Kronecker delta. This expression assumes that the training set \mathbb{T} contains equal numbers of events of all classes. If this is not the case, each $P(\omega_j|\boldsymbol{\xi})$ should be divided by the number of events of class ω_j in the training set and then renormalized to make sure they sum up to 1.

The probability density values $P(\omega_j|\boldsymbol{\xi})$, as defined above, give a continuous classification result with $\sum_{j=1}^l P(\omega_j|\boldsymbol{\xi}) = 1$. A simple way to obtain a discrete classification result from this, is by classifying event $\boldsymbol{\xi}$ as the class for which

$P(\omega_j|\xi)$ is largest, i.e. assign it to the class that was the most numerous in its k nearest neighbors:

$$S_i(k) = \arg \max_{\omega_j} \{P(\omega_j|\xi_i)\}.$$

Taking the k nearest neighbors of ξ_i means that the volume in which training events are sampled depends on the density of events around ξ_i . This is an advantage of the method, as the flexible volume provides the same statistical precision in the entire parameter space, only depending on the value of k . Note that the KNN algorithm is a type of *instance-based learning*, where the complete calculation is deferred until classification and the training phase consists solely of storing the training set of events. This is a disadvantage of the KNN algorithm, as the training may be fast, but the classification itself is computationally expensive.

Results

When using the KNN algorithm on a binary classification problem ($l = 2$), it is possible to plot a ROC curve of the classification results and use that to judge the classification efficiency. The advantage of using the KNN algorithm in this case is that it takes local features of the parameter distributions into account and can thus provide better classification results if the parameter distributions are not well-suited for the application of a dichotomizer.

For more than two classes it is no longer possible to plot a ROC curve. However, in all cases an $l \times l$ *confusion matrix* can be generated, whose elements are given by

$$M_{ab} = \frac{\sum_i \delta(S_i, \omega_a) \cdot \delta(S_i^T, \omega_b)}{\sum_i \delta(S_i^T, \omega_b)},$$

where index i runs over all events classified, $\{\xi_i, S_i^T\} \in \mathbb{D} \setminus \mathbb{T}$. Each classified event is counted in one element of the matrix, where the column b is determined by its true class and the row a by the class as which it was classified. The denominator in the above expression normalizes the sum of each column to 1. It follows that M_{ab} can be interpreted as the chance that an event of true class ω_b will be classified as ω_a by this classifier.

Note that the ROC curve treated in the previous section can be described as interpreting the elements of a single column of the confusion matrix as a two-dimensional vector in ROC space, in the case of two classes.

The diagonal elements of the confusion matrix give fractions of events classified correctly. Assuming equal numbers of events of all classes, the average of the diagonal elements gives the fraction of all events classified correctly. Thus define the following as a measure of the total classification efficiency:

$$I = \frac{1}{l} \sum_{a=1}^l M_{aa} = \frac{1}{l} \text{tr}(M). \quad (5.2)$$

The off-diagonal elements represent events classified incorrectly and their magnitudes show what kind of classification errors occur most frequently.

The classification efficiency depends on the value chosen for k . The optimal value depends on the number of events in the test set \mathbb{T} , the dimension m of the chosen parameter space and the local features of the event distribution in

this space. During this project, for each classification attempt, multiple values of k were taken and the one with the best results was used. In all cases, 90% of the total number of events was taken as the training set and the remaining 10% was used for classification.

Normalization

Because the KNN method as described uses the Euclidean distance in the parameter space to find the k closest neighbors, it is important that the different parameters spanning this space are normalized to have similar¹⁴ length scales. If no normalization is applied, the parameter with the smallest length scale will bias the classification, possibly overruling the effect of adding the other parameters.

For this project, parameter values were normalized by subtracting the average value in the training set and then scaling by the inverse of the standard deviation calculated from the sample variance. For each dimension i of the parameter space:

$$\xi_i \rightarrow \frac{1}{\sigma_{\mathbb{T}}}(\xi_i - \bar{\xi}_{\mathbb{T}}).$$

¹⁴Or rather, the various parameters should ideally have length scales corresponding to their importance in the classification, but this is hard to quantify.

Chapter 6

Results

In this chapter the results of the analysis of this project will be described. Spectra of the most important parameters of those described in Chapter 4 will be given, with a discussion of their power in classifying events.

The parameters will be treated in the same order as they appeared in Chapter 4. ROC curves will be given to show the separation power of individual parameters in distinguishing between photon and neutral pion events, i.e. one-photon and two-photon clusters, since investigating this classification problem was the main objective of this thesis. In the last sections of this chapter, combinations of parameters will be tested using the KNN algorithm and the effects of adding neutron events to the classification problem will also be treated.

General remarks

For all plots in this chapter where the momentum dependence of a quantity is plotted (with the exception of scatter plots), a moving momentum window with a width of $1 \text{ GeV}/c$ was used to select a subset of events for each point of the curve. Although the momentum of events was obtained from the Monte Carlo information, for photons and neutral pions very similar plots can be obtained by plotting the quantities as a function of the total cluster energy, E_{cluster} . For photons, the cluster energy is equal to the momentum of the originating photon, with some smearing due to energy losses and the energy resolution of the detector. For neutral pions the same applies, with the difference that the mass of the pion causes the total cluster energy to be higher than the momentum of the originating pion. However, this difference is very small at the momenta where merged clusters appear.

In this chapter, the ROC integral over the full simulated momentum range is used as a measure to compare parameters, even though the simulated momentum distribution is not very realistic. Because most of the parameters have similar momentum dependencies, i.e. at low momentum they work well, but their separation efficiency drops gradually at high momentum, this was deemed to be an acceptable way of comparing the overall efficiency of parameters. Plots of the momentum dependence of the ROC integral will be given for a selection of parameters and these can be used for a more detailed comparison. In addition, the ROC integrals at three specific momentum ranges can be found in Appendix A for all parameters. By dividing the data sets into multiple sub-

sets, analyzing these subsets separately and comparing the obtained results, the mean error in the ROC integral values given was estimated to be less than 0.001.

The results shown in the plots of the momentum dependence of the ROC integral of a parameter can give better separation efficiencies than the ROC integral over the full momentum range implies. This is due to the way the momentum dependence plot is generated, which effectively includes the information of the momentum of particles in the classification process. As mentioned before, the total cluster energy E_{cluster} can be used to obtain similar results using only information that is experimentally available.

6.1 Bump parameters

6.1.1 Bump multiplicity

The bump multiplicity could in principle be used for efficiently distinguishing between single-photon and two-photon clusters, because the expected number of bumps would naturally be one and two respectively. However, the separation power this parameter provides is in practice not as good as naively expected, since the bump-splitting algorithm described in Section 3.2.3 will not find two bumps that lie too close together and can also find small secondary bumps due to irregularities in the shower shape.

The top row of Figure 6.1 shows the distribution of the bump multiplicity. For the forward end-cap data set, most one-photon clusters indeed have one bump and most two-photon clusters have two, as expected. For the barrel data set, a significant fraction of the two-photon clusters has only a single bump. These come mostly from the higher momenta region as the mean bump multiplicity as a function of momentum plotted in the middle row of Figure 6.1 shows. Only below 4 GeV/ c most pion events have two bumps for the barrel data set, but even in this momentum region not always both bumps are identified. This is a result of the dependence on the bump-splitting algorithm: the granularity of the EMC is not sufficient for it to reliably identify all bumps at higher momenta. The plotted means also show that the number of secondary bumps increases with momentum. The neutron clusters can have various numbers of bumps, increasing with momentum, indicating that these hadronic showers have more irregular shapes than the electromagnetic showers induced by photons.

It is possible to slightly improve the parameter by applying an energy threshold before secondary bumps are counted, i.e. only count secondary bumps with an energy of $E_{\text{bump}} > E_{\text{threshold}}$ (in addition to the default energy threshold of bumps as described in Section 3.2.3). Different energy thresholds were investigated and a threshold of the order of 100 MeV gave the largest ROC integral over the full momentum range. A threshold depending on the cluster energy did not seem promising to improve the results, but because of the large threshold value, some adjustment might be needed for low-momentum events.

The mean bump multiplicity after applying a threshold of 100 MeV is also plotted in the middle row of Figure 6.1. The threshold removes most secondary bump counts and thereby significantly reduces the variance (not plotted) of the number of bumps for photons and pions. Particularly for the forward end-cap data set the threshold improves the separation power of the bump multiplicity. For the barrel data set the momentum region where the secondary bumps form

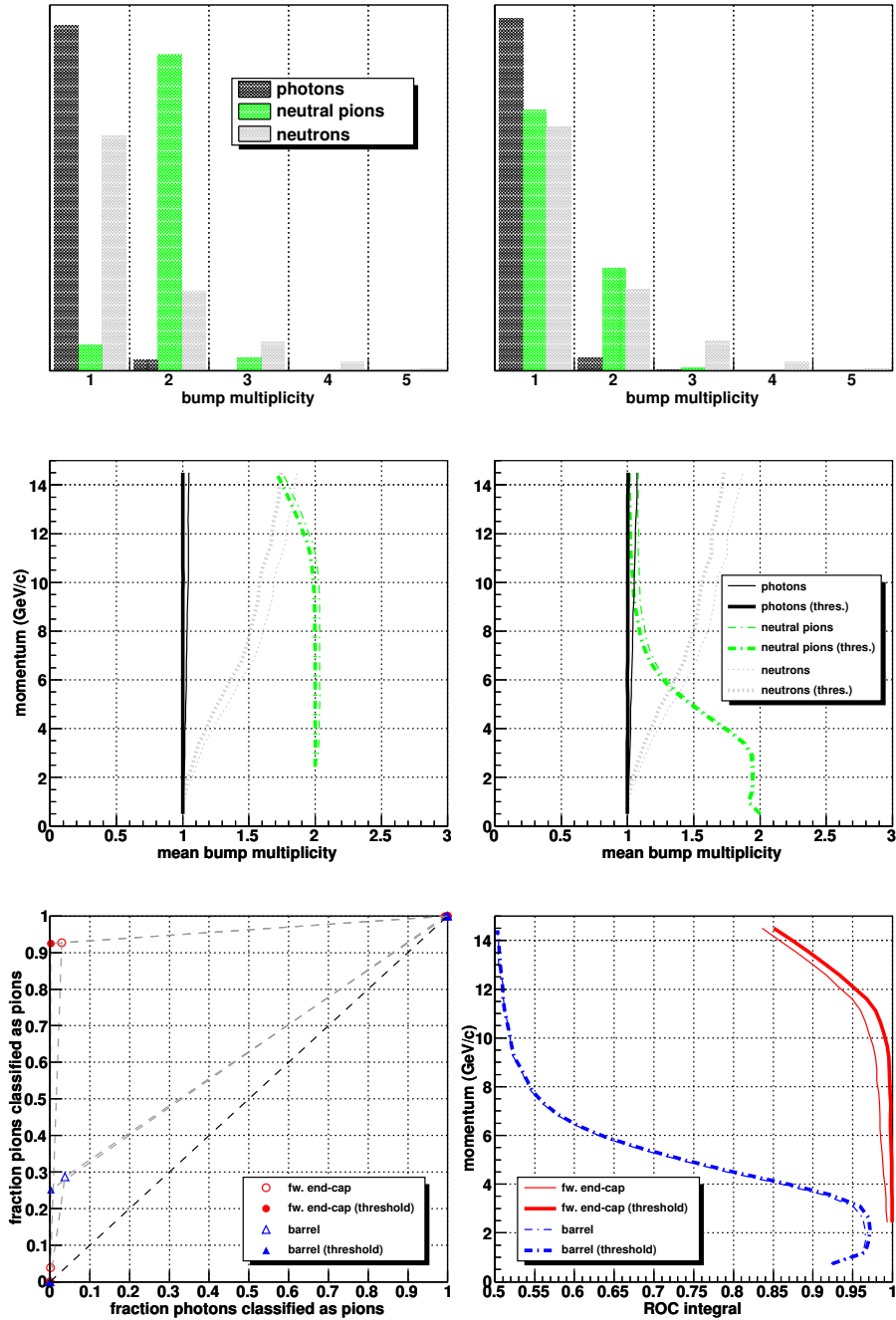


Figure 6.1 – (*Top row*) bar graphs of the bump multiplicity over the full momentum range and (*middle row*) plots of the momentum dependence of the mean bump multiplicity, optionally with a threshold of 100 MeV, for the forward end-cap (*left*) and barrel data sets (*right*). (*Bottom row*) ROC plot of the bump multiplicity over the full momentum range (*left*) and momentum dependence of the ROC integral (*right*), for photon–pion separation.

the main source of misclassifications is too small to show a significant improvement. Note that the threshold does not help in the cases where the opening angle between two photons from a neutral pion decay is small and only a single bump is detected. Because these events cause the majority of misclassifications, the improvement due to the energy threshold is limited.

The ROC curves shown in the bottom row of Figure 6.1 correspond to using the bump multiplicity for the separation of photon and neutral pion events. Note that this discrete-valued parameter gives only a limited number of points in ROC space, which makes the ROC integral from equation (5.1) ill-defined. To still allow a comparison with other parameters, the ROC integral was computed by a linear interpolation of the ROC points.

For each data set there is only one point in ROC space corresponding to a reasonable classification result: these points represent classifying events with one bump as photons and those with multiple bumps as pions. The plot of the momentum dependence of the ROC integral shows that the bump multiplicity gives good classification results for the forward end-cap data set, especially after applying an additional energy threshold of 100 MeV. For the barrel data set, the classification power falls rapidly above 4 GeV/ c . The value of the ‘ROC integral’ over the full momentum range is given in the table below.

Parameter	ROC integral	
	fw. end-cap	barrel
bump multiplicity	0.950	0.624
bump multiplicity with $E_{\text{threshold}} = 100$ MeV	0.962	0.627

6.1.2 Invariant mass reconstruction

The separation power of the bumps can be improved by including the information on their positions and energies. For the two photons from a neutral pion decay these are related according to equation (4.1). This expression was evaluated for clusters with at least two bumps and compared with the actual invariant mass of the neutral pion. The two most energetic bumps of the clusters were taken. It can be argued that it would be better to try all combinations of bumps and look for masses close to the pion mass. However, since neutral pion clusters with more than two bumps did not form the main source of misclassifications, this was not investigated. The additional energy threshold for bumps as described in the previous section was also not used in this case. Clusters with only a single bump were always classified as photons for the generation of ROC plots.

As can be seen from the histograms of the top row of Figure 6.2, the neutral pion events produce a clear peak around the invariant mass of the neutral pion, $m_{\pi^0} = 134.98$ MeV/ c^2 , while there are peaks at lower masses for the photons and neutrons. Fitting the neutral pion peaks with a Gaussian (also plotted) gives $m = 0.132 \pm 0.007$ GeV/ c^2 and $m = 0.13 \pm 0.01$ GeV/ c^2 for the forward end-cap and barrel data sets, respectively. Some energy is missing, which was to be expected, since no effort was made to compensate for energy leakage.

The histograms plotted contain only events that had at least two bumps. For the barrel data set the neutral pion peak thus consists of only about a third of the pion events, mostly with lower momenta as the plots of the middle row of

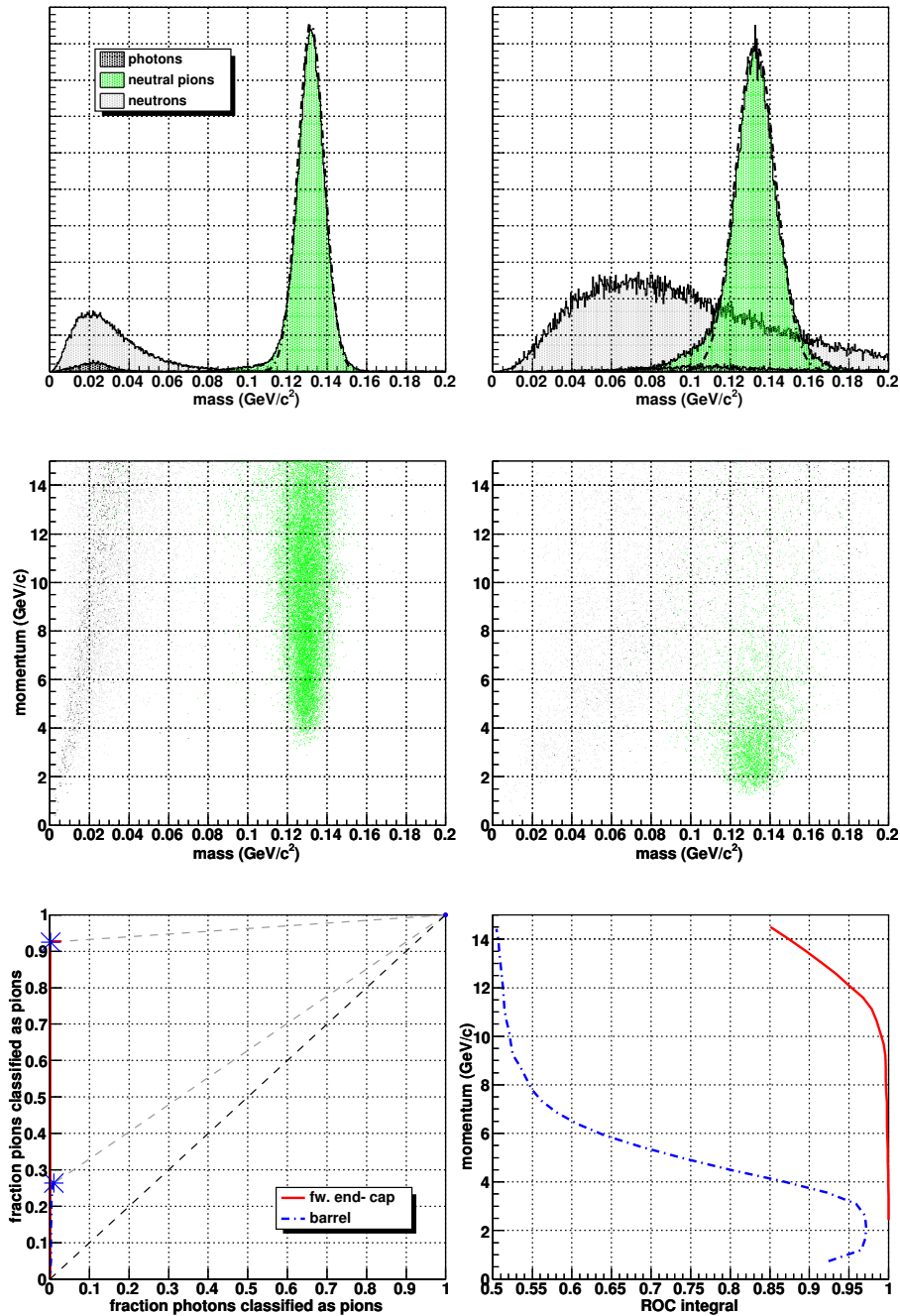


Figure 6.2 – (Top row) histograms of the invariant mass reconstruction over the full momentum range and (middle row) plots of its momentum dependence, for the forward end-cap (left) and barrel data sets (right). Note that only events with multiple bumps are visible in the spectra. (Bottom row) ROC plot of the parameter over the full momentum range (left) and momentum dependence of the ROC integral (right), for photon–pion separation. The indicated points in the ROC plot lie the furthest from the diagonal.

Figure 6.2 clearly show. These plots also show that the width of the neutral pion mass peak increases with momentum and its mean decreases slightly, indicating that at high momentum more energy of the two photons is lost.

The ROC plots for the neutral pion–photon separation at the bottom row of Figure 6.2 show that the invariant mass reconstruction works well at low momentum, but its performance decreases with higher momentum, especially for the barrel data set. Note that the ROC curves are not connected to the point (1, 1), which is due to all the events with only a single bump, which are indivisible. Comparing these plots to the ROC plots of Figure 6.1 shows that the invariant mass reconstruction performs only slightly better than using the bump multiplicity. This is due to the fact that the mass reconstruction method is still unable to identify neutral pion events where only a single bump was found by the bump-splitting algorithm. The main feature of this method is that it can distinguish between a one-photon cluster with two bumps and a two-photon cluster with two bumps.

The ROC integral of the invariant mass reconstruction over the full momentum range, calculated using the same linear interpolation method as for the bump multiplicity, is given in the table below.

Parameter	ROC integral	
	fw. end-cap	barrel
invariant mass reconstruction	0.962	0.628

6.1.3 Concluding remarks (bump parameters)

As described in Section 5.1.1, the maximum momentum of events for the barrel part of the EMC is about 7 GeV/c, but the classification efficiency of the invariant mass reconstruction and bump multiplicity already falls significantly before reaching this level. Also for the forward end-cap, where events up to a maximum momentum of about 14 GeV/c are possible, the classification efficiency drops at higher momenta. This makes it interesting to investigate other classification parameters that do not rely on the number of bumps, but instead take all the digis of a cluster into account. The results of using the other possible cluster parameters will be described in the rest of this chapter.

6.2 Shower shape parameters

6.2.1 Cluster energy fractions

The first parameters based on digis that was investigated is the ratio between the energy in several groups of digis and the total cluster energy, as defined by equation (4.2). In Figure 6.4 the results for the energy fraction in the four most energetic digis are plotted. This parameter $f_{\max,4}$ gives the best results out of the investigated parameters $f_{\max,n}$, as shown by the ROC integrals as a function of n plotted in Figure 6.3.

The $f_{\max,4}$ spectra show clear peaks for the one-photon and two-photon clusters, where the latter have a smaller fraction of the total cluster energy in the four most energetic digis due to their larger spread in energy. The neutron clusters cover again a wider range of energy fractions. For the forward end-cap

data set the momentum dependence of this parameter is small for the neutral pions and photons. For the barrel data set there is a considerable overlap between the photon and neutral pion events, mostly at higher momenta.

The ROC plots show that $f_{\max,4}$ provides better separation power between neutral pions and photons than the methods based on bumps described in the previous section. The ROC curves of $f_{\max,4}$ are also more symmetric in the identification efficiencies of photons and neutral pions. The separation efficiency is good for the forward end-cap data set, although there are misclassifications at all momenta. For the barrel data set, the parameter provides good separation results up to about 6 GeV/c.

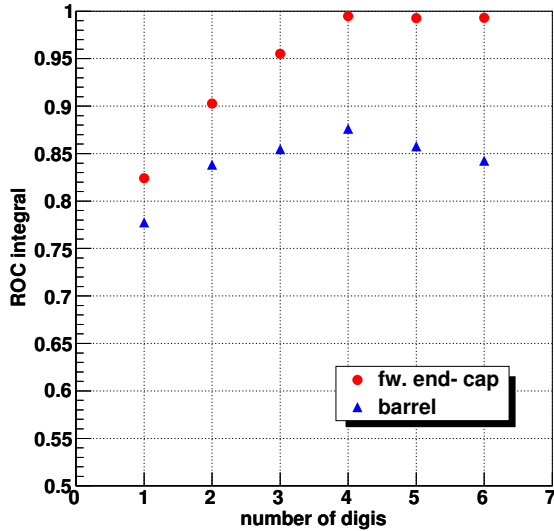


Figure 6.3 – ROC integral of $f_{\max,n}$ over the full momentum range for different values of n .

Of all the other energy fractions based on digis, defined by equation (4.3), the best results are given by $f_{\square,9}$, the energy fraction in the central 3×3 digis of a cluster. The results of this parameter are given in Figure 6.5 and are somewhat similar to those of $f_{\max,4}$. However, with the exception of the high momentum region for the barrel data set, the variation in this energy fraction for the neutral pion events is much larger. In the high momenta region for the barrel data set, the neutral pions do not deposit much energy outside the central nine crystals anymore and the fraction of the total cluster energy deposited in them becomes close to unity.

The parameter $f_{\square,9}$ gives slightly better separation results between photons and neutral pions for the forward end-cap data set in comparison with $f_{\max,4}$. Interestingly, the parameter gives a better separation efficiency for the barrel data set at low momentum, but the efficiency falls rapidly after 4 GeV/c giving a worse overall separation efficiency for the barrel data set than in the case of $f_{\max,4}$.

The energy fraction in the central 5×5 digis of the cluster $f_{\square,25}$ gives similar

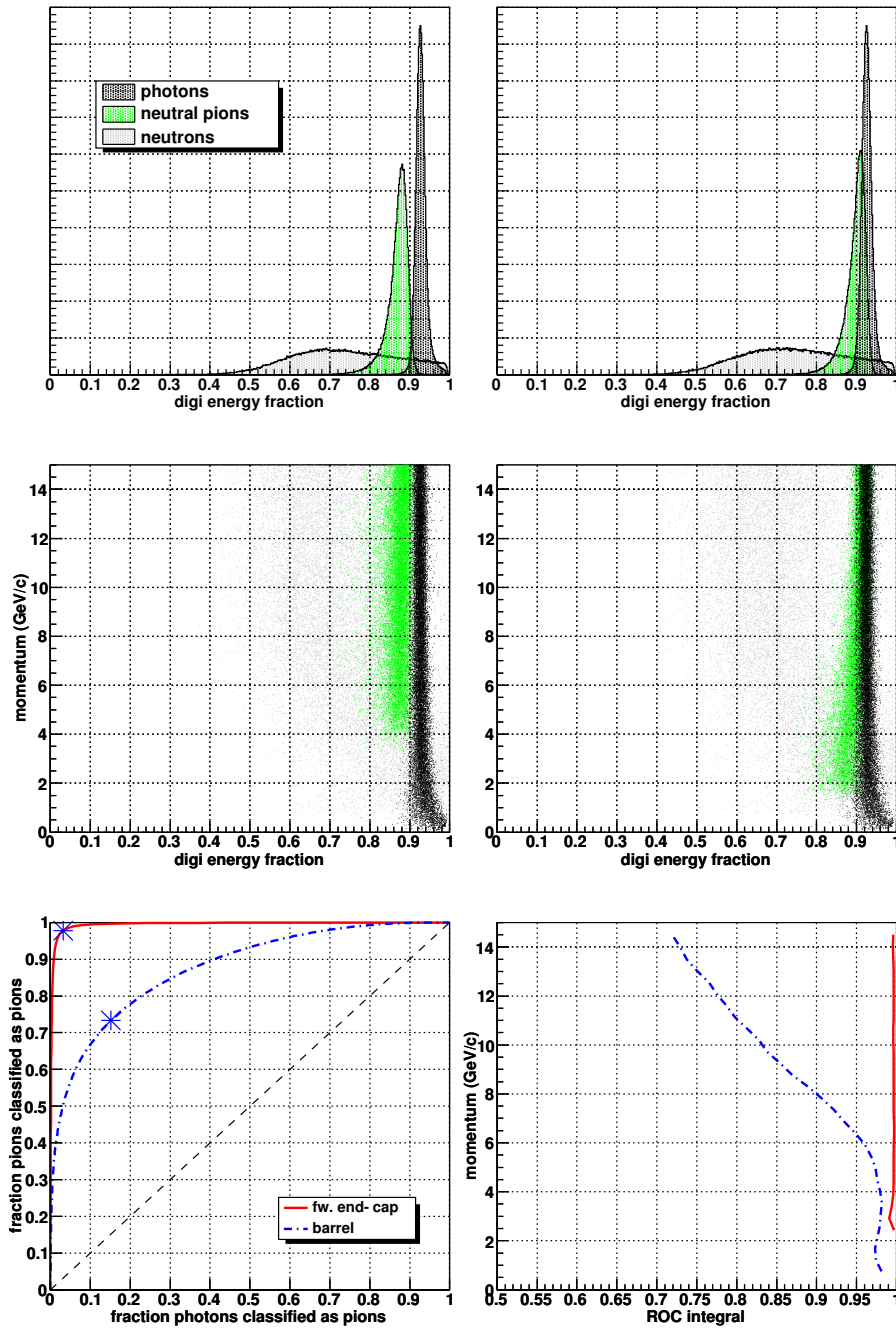


Figure 6.4 – (Top row) histograms of the energy fraction in the four most energetic digis $f_{\max,4}$ over the full momentum range and (middle row) scatter plots of its momentum dependence, for the forward end-cap (left) and barrel data sets (right). (Bottom row) ROC plot of the parameter over the full momentum range (left) and momentum dependence of the ROC integral (right), for photon–pion separation. The indicated points in the ROC plot lie the furthest from the diagonal.

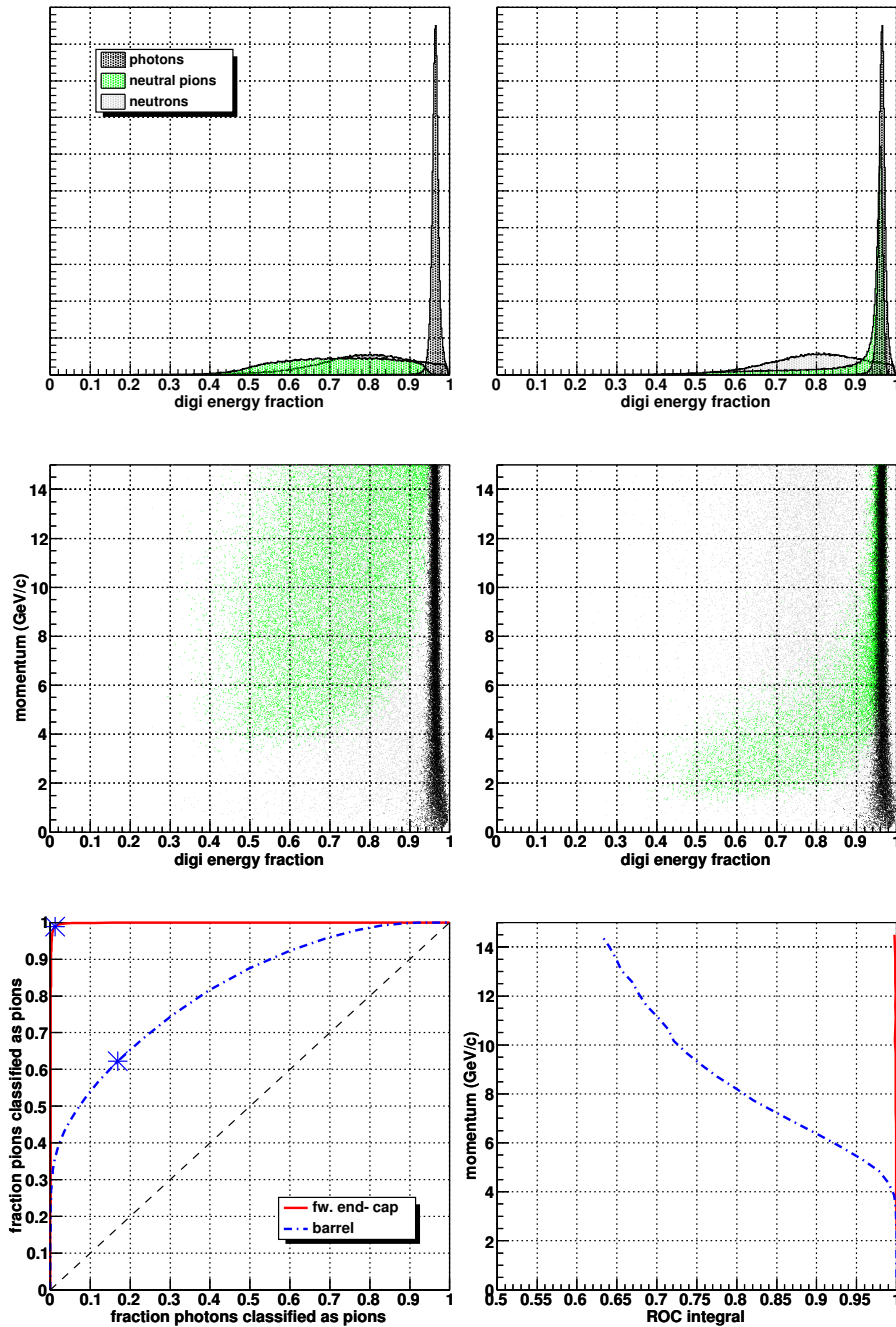


Figure 6.5 – (Top row) histograms of the energy fraction in the central 3×3 digis $f_{\square 9}$ over the full momentum range and (middle row) scatter plots of its momentum dependence, for the forward end-cap (left) and barrel data sets (right). (Bottom row) ROC plot of the parameter over the full momentum range (left) and momentum dependence of the ROC integral (right), for photon–pion separation. The indicated points in the ROC plot lie the furthest from the diagonal.

results as $f_{\square 9}$, with worse separation efficiency at high momentum. Quotients of the energies¹⁵ $E_{\square 1}$, $E_{\square 9}$ and $E_{\square 25}$ do not give very good separation results.

The ROC integrals over the full momentum range of all digi energy fractions discussed in this section are given in the table below.

Parameter	ROC integral	
	fw. end-cap	barrel
energy fraction in most energetic digi, $f_{\max,1} = f_{\square 1}$	0.824	0.777
energy fraction in two most energetic digis, $f_{\max,2}$	0.903	0.838
energy fraction in three most energetic digis, $f_{\max,3}$	0.955	0.855
energy fraction in four most energetic digis, $f_{\max,4}$	0.995	0.876
energy fraction in five most energetic digis, $f_{\max,5}$	0.993	0.858
energy fraction in six most energetic digis, $f_{\max,6}$	0.993	0.842
energy fraction in central 3×3 digis, $f_{\square 9}$	0.998	0.819
energy fraction in central 9×9 digis, $f_{\square 25}$	0.989	0.748
quotient of central energy fractions, $E_{\square 1}/E_{\square 9}$	0.507	0.696
quotient of central energy fractions, $E_{\square 9}/E_{\square 25}$	0.842	0.772
quotient of central energy fractions, $E_{\square 1}/E_{\square 25}$	0.645	0.747

6.2.2 Cluster mass

The distributions of the cluster mass parameter m_{cluster} as defined by equation (4.4) are plotted in Figure 6.6. For the photon events, the cluster mass depends approximately linearly on momentum. For the neutral pion events, the parameter gives larger values and is also increasing with momentum. This results in a peak for the neutral pions and a broad distribution for the photons, with little overlap in the case of the forward end-cap data set. For the barrel data set, both the photon and pion distributions are broad, with significant overlap. The neutron events have similar values for the cluster mass as photon events, although their distribution is different.

As the ROC plots in Figure 6.6 show, the cluster mass parameter provides decent separation results between photons and pions when using a single cut for the forward end-cap data set, but less so for the barrel data set. For the latter data set, the separation between photon and neutral pion events all but disappears at the higher momenta range.

Since the cluster mass parameter has a strong momentum dependence, combining it with other parameters will improve the results. Good results can be obtained by combining it with the total cluster energy E_{cluster} , that is approximately equal to the momentum of photons or (at high momentum) neutral pions.

The ROC integral of the cluster mass over the full momentum range is given in the table below.

Parameter	ROC integral	
	fw. end-cap	barrel
cluster mass, m_{cluster}	0.998	0.678

¹⁵Or equivalently, quotients of $f_{\square 1}$, $f_{\square 9}$ and $f_{\square 25}$

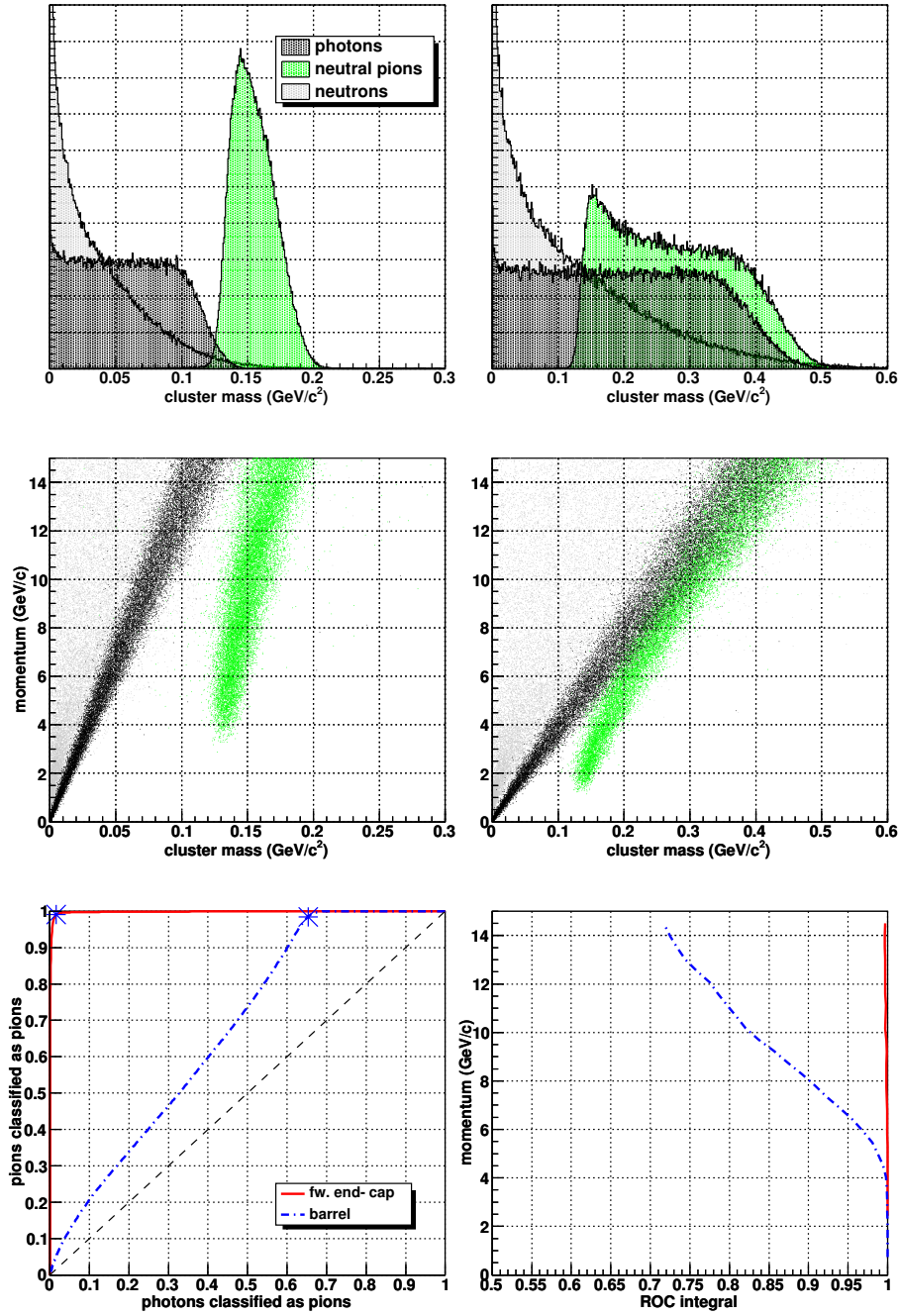


Figure 6.6 – (Top row) histograms of the cluster mass m_{cluster} over the full momentum range, and (middle row) scatter plots of its momentum dependence, for the forward end-cap (left) and barrel data sets (right). (Bottom row) ROC plot of the parameter over the full momentum range (left) and momentum dependence of the ROC integral (right), for photon–pion separation. The indicated points in the ROC plot lie the furthest from the diagonal.

6.2.3 Cluster moments

The first and second cluster moments as defined by expression (4.5) of the variables θ , ϕ and r were tested for their classification efficiency. The best results are obtained from the second lateral cluster moment $\langle r^2 \rangle$, plotted in Figure 6.7. This cluster moment is a measure of the radial energy distribution of a cluster: a larger value corresponds to a distribution where the energy is deposited further from the cluster center on average.

Neutral pion clusters generally have larger values for the second lateral cluster moment than the more symmetric photon clusters where the energy is deposited closer to the cluster center. Both event types have a well-defined peak depending on the momentum. For the simulated photon events the value of this cluster moment was not very momentum-dependent, except below 2 GeV/c. For the neutral pion events, however, the cluster moment is very momentum-dependent. The high-momentum events have smaller values due to the smaller opening angles of the two photons of the pion decays resulting in the energy being deposited closer to the cluster center. For the barrel data set, significant overlap between the two distributions occurs upwards from about 6 GeV/c on. The momentum dependence of the parameter results in a sharp peak for the photon events, while the neutral pion events cover a wider range. The distribution of neutron events was again very broad without any well-defined peak.

For the separation of photons and neutral pions the second lateral cluster moment gives good results. The ROC integrals for the various cluster moments over the full momentum range are given in the table following. This includes the normalized lateral moments, as given by equation (4.6).

Parameter	ROC integral	
	fw. end-cap	barrel
first lateral cluster moment, $\langle r \rangle$	0.992	0.837
second lateral cluster moment, $\langle r^2 \rangle$	0.999	0.893
first cluster moment of theta, $\langle \theta \rangle$	0.907	0.748
second cluster moment of theta, $\langle \theta^2 \rangle$	0.935	0.807
first cluster moment of phi, $\langle \phi \rangle$	0.921	0.739
second cluster moment of phi, $\langle \phi^2 \rangle$	0.945	0.799
normalized first lateral cluster moment	0.973	0.870
normalized second lateral cluster moment, lat	0.993	0.873

The cluster moments of second order give better results than those of first order. Also, the cluster moments of r , which combine the information from θ and ϕ , give better results than using θ or ϕ apart from each other. Using the normalized lateral cluster moments (not plotted) does not improve the separation power between photons and neutral pions in most cases. However, it does improve the separation between neutrons and the other particle types, but this is of lesser importance for this thesis.

6.2.4 Zernike moments

The Zernike moments defined by equation (4.7) were evaluated for various combinations of the subscripts m and n . The best results are obtained with Zernike

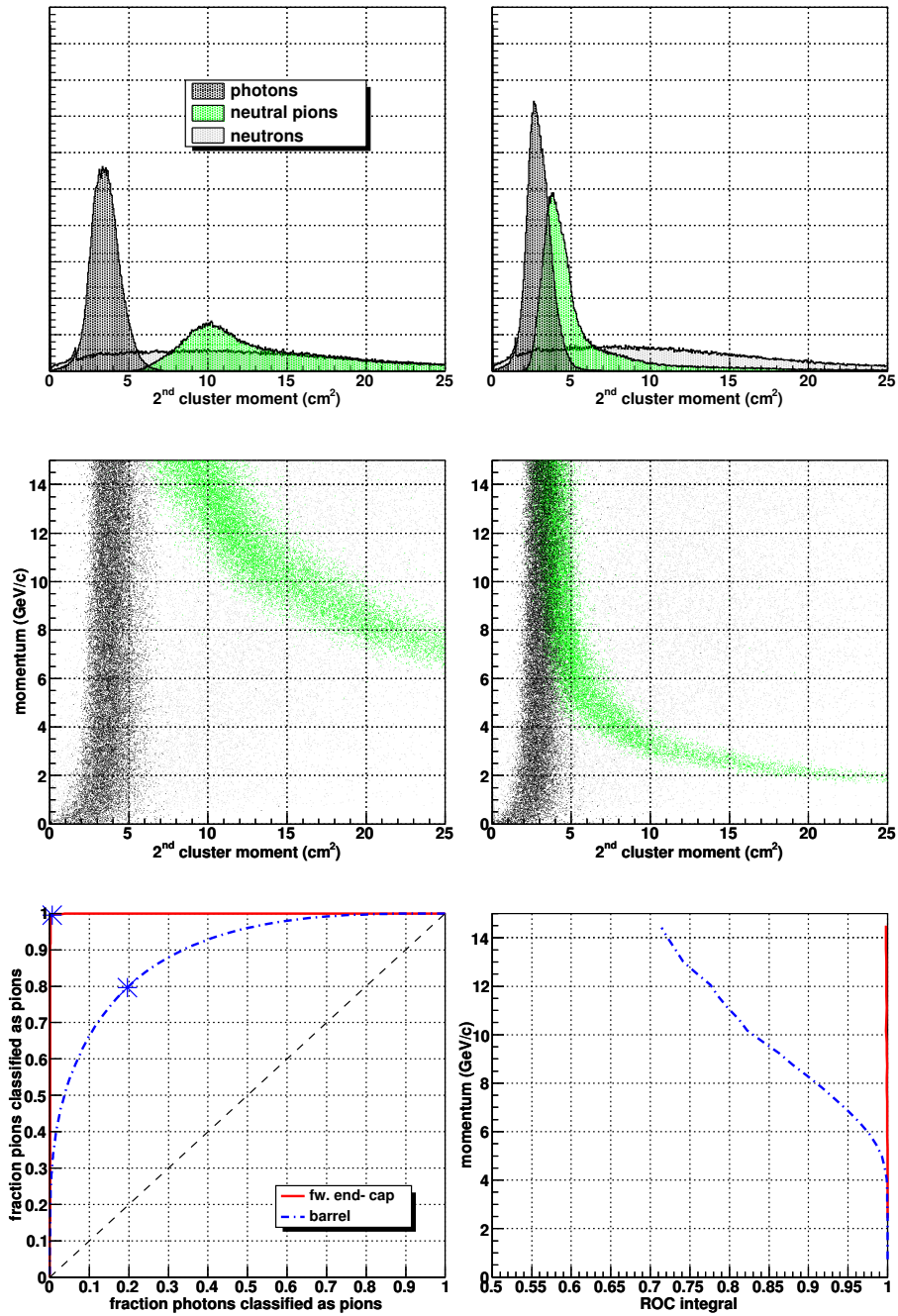


Figure 6.7 – (Top row) histograms of the second lateral cluster moment $\langle r^2 \rangle$ over the full momentum range, and (middle row) scatter plots of its momentum dependence, for the forward end-cap (left) and barrel data sets (right). (Bottom row) ROC plot of the parameter over the full momentum range (left) and momentum dependence of the ROC integral (right), for photon–pion separation. The indicated points in the ROC plot lie the furthest from the diagonal.

moment Z_2^0 , plotted in Figure 6.8. For these plots, the radial normalization constant was taken as $\rho_0 = 15$ cm. Note the similarity of these results with the results of the second lateral cluster moment treated in the previous section. The Zernike moment Z_2^0 is virtually the same quantity, although normalized and reversed. These two parameters are thus highly correlated and using them both during classification would not be very useful. The second cluster moment performs slightly better, possibly because the normalization of the radial distance of digis during the calculation of the Zernike moment leads to the exclusion of all digis at a distance larger than ρ_0 from the cluster center.

The influence of the normalization distance ρ_0 on the classification results is limited, unless it is taken too small and only a few digis are used in the calculation of the Zernike moment. Although it simply scales the coordinate system, the ρ -dependence of the Zernike moments can make the choice of ρ_0 important for some of the Zernike moments. For most of the treated Zernike moments, increasing ρ_0 above a certain value does not change the separation efficiency. However, for Zernike moment Z_5^3 increasing ρ_0 does decrease the separation. The default value used in PandaRoot of $\rho_0 = 15$ cm provides good results in all cases that were investigated.

The ROC integrals of Zernike moments for $2 \leq n \leq 5$ over the full momentum range are given in the table below.

Parameter	ROC integral	
	fw. end-cap	barrel
Zernike moment Z_2^0 with $\rho_0 = 15$ cm	0.999	0.890
Zernike moment Z_2^2 with $\rho_0 = 15$ cm	0.997	0.816
Zernike moment Z_3^1 with $\rho_0 = 15$ cm	0.925	0.617
Zernike moment Z_3^3 with $\rho_0 = 15$ cm	0.960	0.689
Zernike moment Z_4^0 with $\rho_0 = 15$ cm	0.997	0.885
Zernike moment Z_4^2 with $\rho_0 = 15$ cm	0.987	0.820
Zernike moment Z_4^4 with $\rho_0 = 15$ cm	0.958	0.666
Zernike moment Z_5^1 with $\rho_0 = 15$ cm	0.929	0.605
Zernike moment Z_5^3 with $\rho_0 = 15$ cm	0.970	0.717
Zernike moment Z_5^5 with $\rho_0 = 15$ cm	0.891	0.650

As mentioned before, the Zernike moment Z_2^0 gives the best results, but is closely linked to the second lateral cluster moment (with a correlation coefficient in absolute value larger than 0.99). Most of the even-numbered Zernike moments in the above table are highly correlated. The next-best moments, Z_2^2 , Z_4^0 and Z_4^2 , are all correlated to Zernike moment Z_2^0 with coefficients larger than 0.95. Therefore no significant improvement is to be expected when combining these moments with the second lateral cluster moment.

The odd-numbered Zernike moments are more interesting to use in combination with other parameters. The best one to choose is the Zernike moment Z_5^3 . Although still correlated with a coefficient of about 0.8, it contains sufficient uncorrelated information to provide some improvement when used in combination with other parameters.

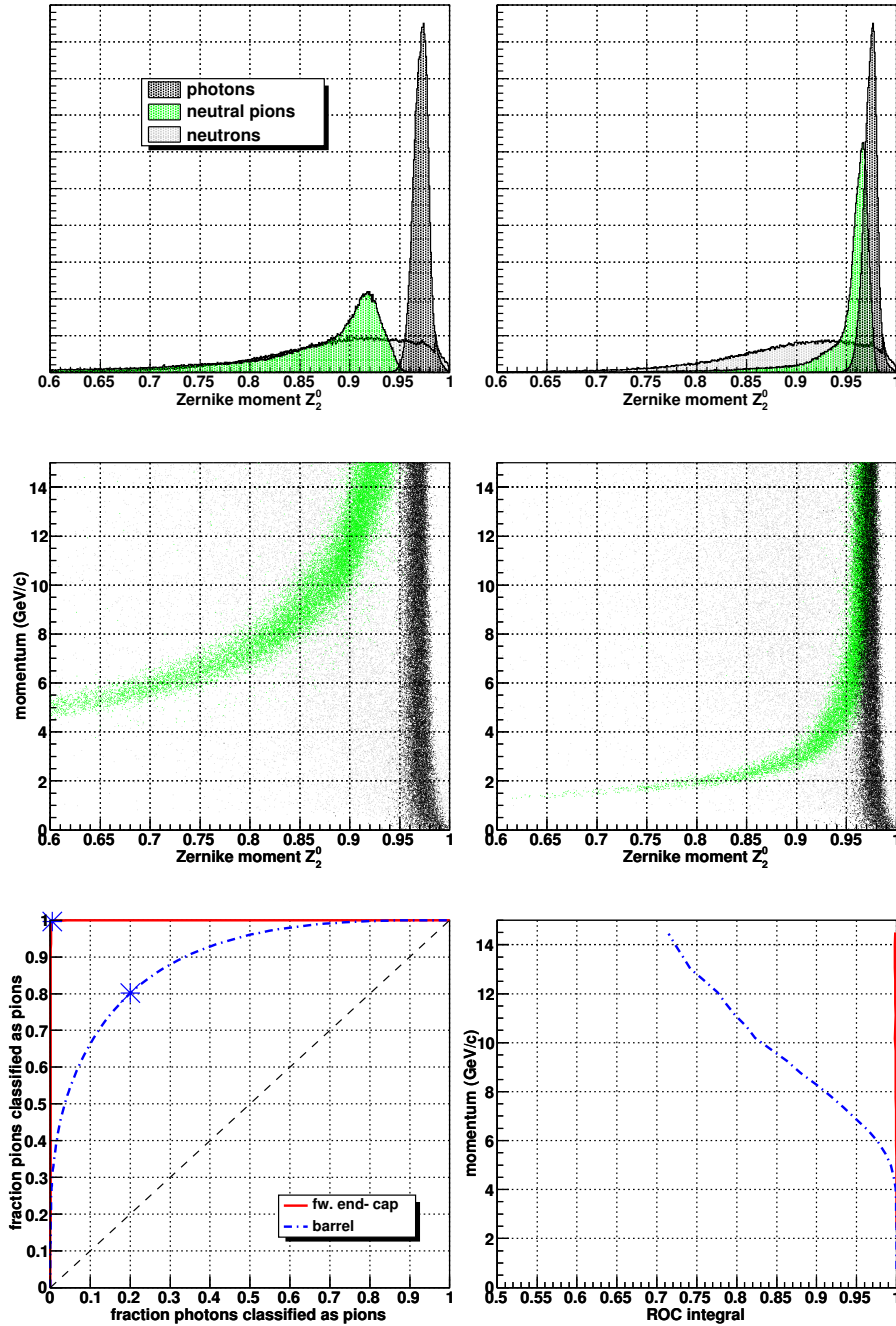


Figure 6.8 – (Top row) histograms of Zernike moment Z_2^0 over the full momentum range, and (middle row) scatter plots of its momentum dependence, for the forward end-cap (left) and barrel data sets (right). (Bottom row) ROC plot of the parameter over the full momentum range (left) and momentum dependence of the ROC integral (right), for photon–pion separation. The indicated points in the ROC plot lie the furthest from the diagonal.

6.2.5 Eccentricity

The major and minor cluster moments defined by equation (4.8) were calculated using the method described in Section 4.3.5. The results of the second moment of distance to the minor axis $\langle r_{\text{minor}}^2 \rangle$ are given in Figure 6.9. The shape of the spectra is again similar to those of the second lateral cluster moment, giving approximately the same separation power between photons and neutral pions.

Results for the ‘eccentricity integral’ defined by equation (4.10) are plotted in Figure 6.10. As expected the neutral pion clusters are rated as less radially symmetric than the photon clusters. With increasing momentum the neutral pion clusters get less asymmetric due to smaller opening angles, while the photon clusters get more asymmetric and the neutron clusters are somewhat in-between. For the barrel data set, both photon and neutral pion clusters have a wide distribution at higher momenta, resulting in a considerable overlap.

The ROC integrals over the full momentum range of the parameters treated in Section 4.3.5 are given in the table below.

Parameter	ROC integral	
	fw. end-cap	barrel
first major cluster moment, $\langle r_{\text{major}} \rangle$	0.746	0.729
second major cluster moment, $\langle r_{\text{major}}^2 \rangle$	0.744	0.737
first minor cluster moment, $\langle r_{\text{minor}} \rangle$	0.992	0.815
second minor cluster moment, $\langle r_{\text{minor}}^2 \rangle$	0.999	0.886
epsilon, $\epsilon_{\text{cluster}}$	0.985	0.734
eccentricity integral, $\mathcal{J}_{\text{cluster}}$ with $\Delta\rho = 1$ cm	0.998	0.857

The second moments again give better results than those of first order, although the difference is smaller than with the other cluster moments. The moments of distance to the minor axis give much better results than the moments of distance to the major axis. This makes sense as the neutral pion clusters consists of two neighboring photon showers. From the perspective of the direction of the major axis, the two showers cover each other and the resulting shape should look similar to that of a single photon shower. Note that the second minor cluster moment is also highly correlated with the second lateral cluster moment with a correlation coefficient larger than 0.99.

As mentioned in Section 4.3.5, the calculation of the major and minor moments done in this project is different from the one implemented in PandaRoot. In PandaRoot, a linear least-squares fitting is done that minimizes vertical rather than perpendicular offsets and instead of a local two-dimensional coordinate system, the θ - and ϕ -positions of the digis are used. For the barrel data set, the two methods give similar efficiencies. For the forward end-cap, the method used in this project gives better results: the second minor moment calculated in PandaRoot gives a ROC integral of 0.956 over the full momentum range.

The eccentricity integral parameter also gives decent results, but not as good as the second minor cluster moment. This parameter also shows a stronger momentum dependence for photon events than the various cluster moments described before.

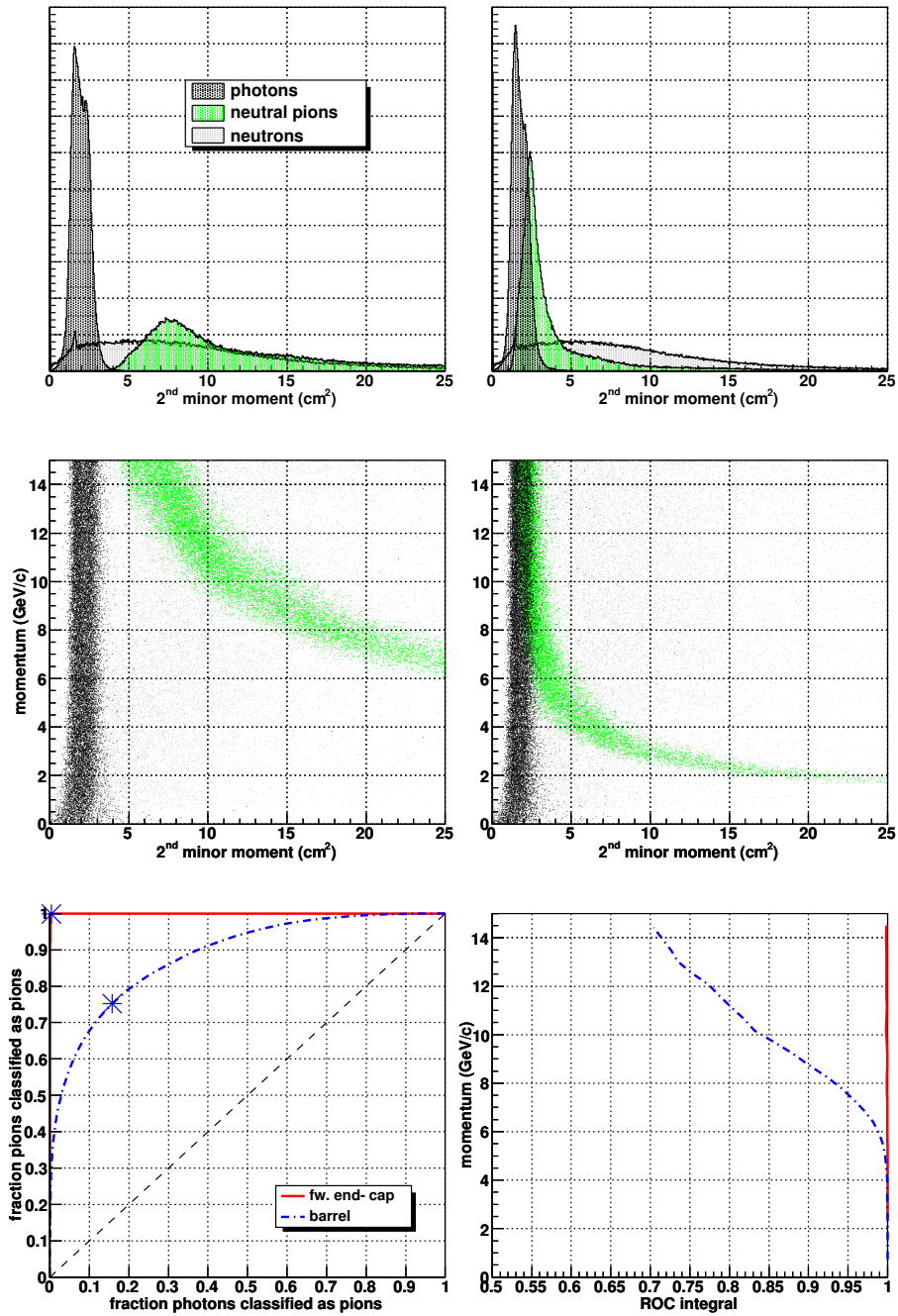


Figure 6.9 – (*Top row*) histograms of second minor cluster moment $\langle r_{\text{minor}}^2 \rangle$ over the full momentum range, and (*middle row*) scatter plots of its momentum dependence, for the forward end-cap (*left*) and barrel data sets (*right*). (*Bottom row*) ROC plot of the parameter over the full momentum range (*left*) and momentum dependence of the ROC integral (*right*), for photon–pion separation. The indicated points in the ROC plot lie the furthest from the diagonal.

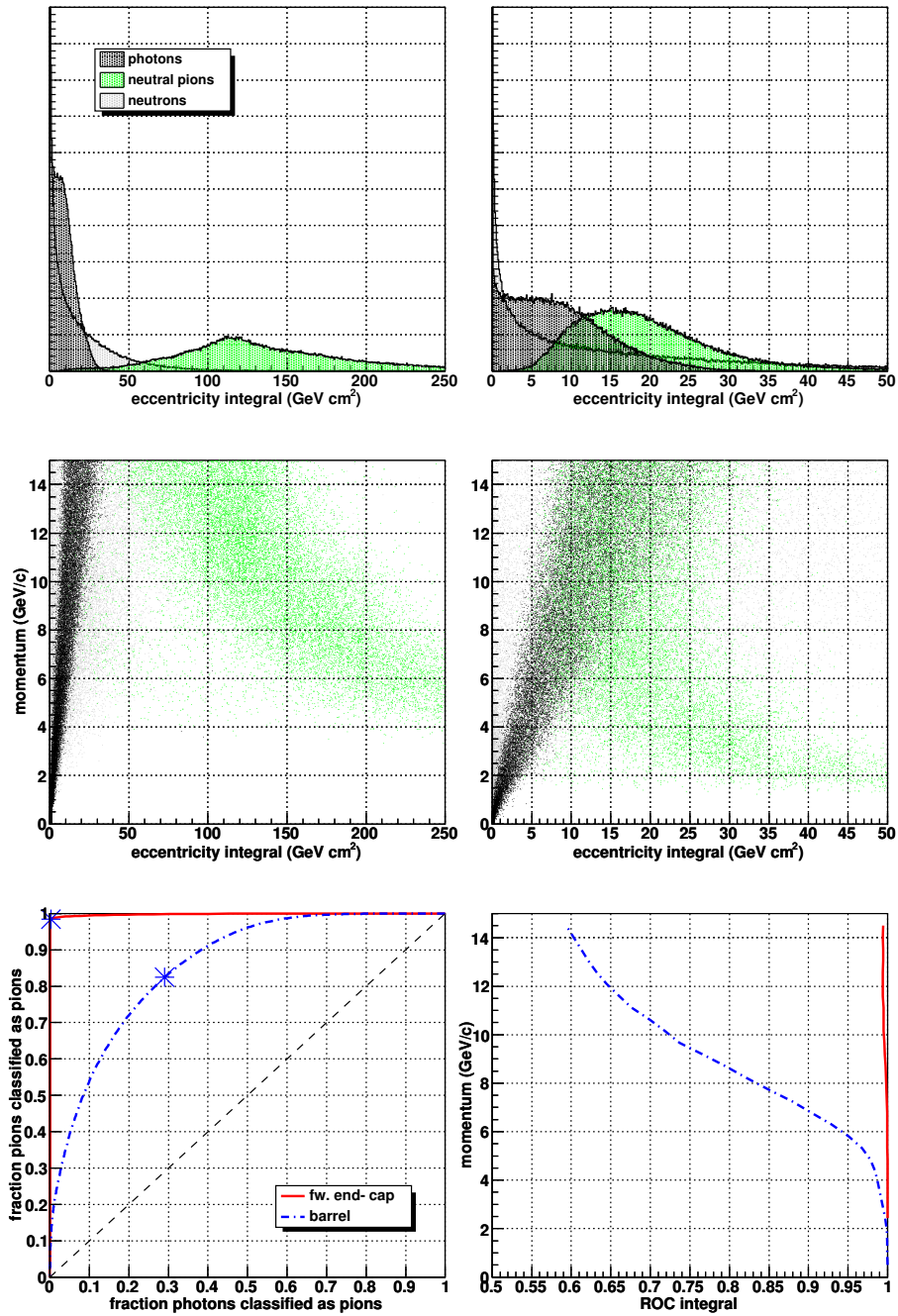


Figure 6.10 – (Top row) histograms of ‘eccentricity integral’ $\mathcal{J}_{\text{cluster}}$ over the full momentum range, and (middle row) scatter plots of its momentum dependence, for the forward end-cap (left) and barrel data sets (right). (Bottom row) ROC plot of the parameter over the full momentum range (left) and momentum dependence of the ROC integral (right), for photon–pion separation. The indicated points in the ROC plot lie the furthest from the diagonal.

6.2.6 Concluding remarks (shower shape parameters)

As the parameters described in the previous sections show, it is quite possible to achieve better separation results than the bump methods described in Section 6.1 give, by using parameters that take all digis of a cluster into account. The best single parameter is the second lateral cluster moment $\langle r^2 \rangle$, and especially for the barrel data set, this parameter gives better results than the invariant mass reconstruction as recapitulated in the table below.

Parameter	ROC integral	
	fw. end-cap	barrel
invariant mass reconstruction	0.962	0.628
second lateral cluster moment, $\langle r^2 \rangle$	0.999	0.893

To allow for a meaningful comparison, the momentum dependence of the classification efficiency of both parameters is also plotted in Figure 6.11 for both data sets.

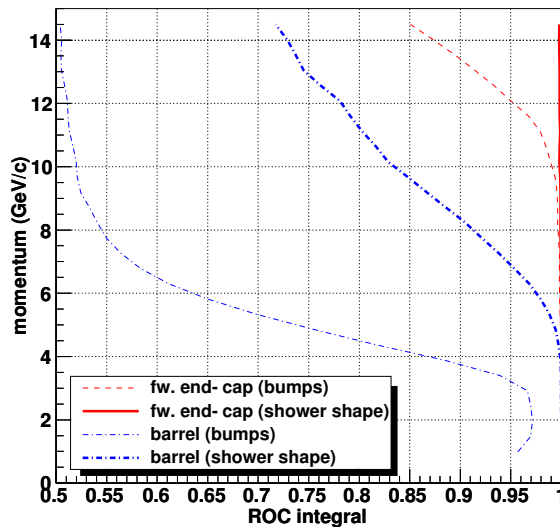


Figure 6.11 – The momentum dependence of the ROC integrals for photon-pion separation for the invariant mass reconstruction (using bumps) and the second lateral cluster moment $\langle r^2 \rangle$ (a shower shape parameter).

For the forward end-cap data set, the invariant mass reconstruction works well and only at the highest momenta the classification efficiency drops somewhat. Note, however, that neutral pions with momenta close to 15 GeV/c are quite rare in the $\bar{\text{P}}\text{ANDA}$ experiment, as mentioned before in Section 5.1.1. The second lateral cluster moment gives almost perfect separation results at any momentum for the forward end-cap.

The invariant mass reconstruction is less effective for the barrel data set, even at lower momenta not reaching a 100% classification efficiency. The second

lateral cluster moment as a classifier works well up to a momentum of about 6 GeV/ c . This might be all the efficiency that is required for this part of the barrel, since pions with higher momentum are rare for the barrel part of the detector. Nevertheless, to investigate the upper limit of the achievable separation efficiency, a multivariate analysis was done for the barrel data set, as will be treated in the next section.

6.3 Multivariate analysis

So far all parameters have been treated individually, but by using the KNN algorithm described in Section 5.2.2, it is possible to combine multiple parameters¹⁶ for photon–pion classification to attempt to increase the efficiency. Of course this only works when the parameters contain some uncorrelated information. The results so far treated have shown that most of the parameters are highly correlated, so huge improvements of separation efficiency should not be expected.

As shown in the previous sections, the binary classification problem of one-photon versus two-photon clusters can be solved satisfactorily for the forward end-cap data set using only the second lateral cluster moment. For the barrel data set, the classification efficiency of single parameters is less and using multiple parameters might be promising. In this project, combinations of some of the best performing single parameters were tried, also including the cluster energy E_{cluster} , as many parameters are momentum-dependent:

$$\{E_{\text{cluster}}, m_{\text{cluster}}, f_{\text{max}4}, \langle r^2 \rangle, Z_5^3, \langle r_{\text{minor}}^2 \rangle, \mathcal{J}_{\text{cluster}}\}.$$

The results for the best-performing combinations of two, three and four parameters from this set are given in the table below. Adding more parameters did not improve the results further and in fact tended to decrease the classification efficiency. The KNN algorithm does not guarantee that adding more parameters actually improves the result.

Parameter	KNN ROC integral	
	fw. end-cap	barrel
$\{E_{\text{cluster}}, \langle r_{\text{minor}}^2 \rangle\}$	1.000	0.937
$\{E_{\text{cluster}}, \langle r_{\text{minor}}^2 \rangle, f_{\text{max}4}\}$	1.000	0.962
$\{E_{\text{cluster}}, \langle r_{\text{minor}}^2 \rangle, f_{\text{max}4}, Z_5^3\}$	0.999	0.964

Note that for the forward end-cap data set using multiple parameters provides little benefit. For the barrel data set there is a significant improvement of using the four parameters listed over just using the lateral cluster moment.

The combinations given in the table above are by no means the only well-performing combinations. Because the parameters involved are highly correlated, there are many combinations that give similar results. For instance, substituting $\langle r^2 \rangle$ for $\langle r_{\text{minor}}^2 \rangle$ or substituting m_{cluster} for E_{cluster} hardly changes the results.

¹⁶The KNN algorithm could also be applied to a single parameter, but this would not be very useful for the treated parameters, since all of them had distributions where the simple dichotomizing classifier used for generating the ROC curves gives good results.

In Figure 6.12 the momentum dependence of the classification efficiency of the set of four parameters $\{E_{\text{cluster}}, \langle r_{\text{minor}}^2 \rangle, f_{\text{max}4}, Z_5^3\}$ for the barrel data set is given in comparison with the efficiencies of the single parameters treated before. Clearly there is some improvement at high momentum over using only the second lateral cluster moment $\langle r^2 \rangle$.

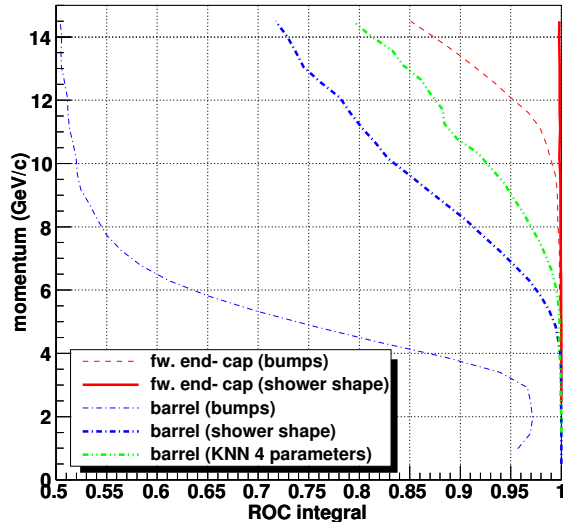


Figure 6.12 – The momentum dependence of the ROC integral for photon-pion separation of using the KNN algorithm with a set of four parameters, in comparison with the ROC integrals of the single parameters given in Figure 6.11.

Although Figure 6.12 demonstrates that a multivariate analysis can improve the classification efficiency for the barrel part of the EMC, it can be questioned whether the result is worth the added complexity of using the KNN algorithm for the problem considered in this thesis. However, when including more than two particle classes, using such an algorithm becomes unavoidable.

6.4 Adding neutrons

In this final section, the effect of adding neutrons to the cluster classification problem is investigated. In the spectra of the treated parameters in the preceding sections, the neutron events were also plotted. From this it is clear that, while photon and neutral pion events typically form narrow distributions in the spectra, neutron events do not, and produce very wide distributions instead. This implies that the most important factor in the classification problem with all three classes is still the separation between photon and neutral pion events, while the overlap with neutron events is similar for most parameters.

Since the ROC integral cannot be used for a classification problem with more than two classes, the average of the diagonal elements of the confusion matrix, as given by equation (5.2), was used as a measure for the classification

efficiency. Note that this measure gives equal priority to all particle classes, but it still gives some indication of the relative classification efficiencies.

6.4.1 Single parameters

Including neutrons in the classification and using the described measure of classification efficiency, the relative performance of the parameters treated in this chapter changes somewhat. Now not only the separation between photons and neutral pions determines the result, but also the overlap with neutron events. For a selection of parameters, the results over the full momentum range are given in the table below.

Parameter	KNN	
	fw. end-cap	barrel
energy fraction in four most energetic digis, $f_{\max,4}$	0.840	0.739
normalized second lateral cluster moment, lat	0.757	0.719
second minor moment, $\langle r_{\text{minor}}^2 \rangle$	0.703	0.693
second lateral cluster moment, $\langle r^2 \rangle$	0.684	0.703
cluster mass, m_{cluster}	0.748	0.602
eccentricity integral, $\mathcal{I}_{\text{cluster}}$ with $\Delta\rho = 1$ cm	0.729	0.562
cluster energy, E_{cluster}	0.631	0.572

The single best parameter is now no longer the cluster moment, but instead the energy fraction in the four most energetic digis, $f_{\max,4}$. Because this parameter is not very momentum-dependent, the overlap of the photon and neutral pion spectra with neutrons is smaller than in the case of the cluster moments, which gives a better rating. Interesting is that the normalization of the second lateral cluster moment significantly improves its results when neutrons are added to the problem.

The complete confusion matrices for a KNN classification using the $f_{\max,4}$ parameter are given by

$$M_{\text{fw. end-cap}} = \begin{pmatrix} 0.95 & 0.03 & 0.02 \\ 0.03 & 0.92 & 0.06 \\ 0.20 & 0.15 & 0.65 \end{pmatrix} \quad \text{and} \quad M_{\text{barrel}} = \begin{pmatrix} 0.82 & 0.16 & 0.02 \\ 0.26 & 0.69 & 0.05 \\ 0.18 & 0.12 & 0.71 \end{pmatrix},$$

where the particle classes are ordered as (γ, π^0, n) . These matrices are clearly diagonally dominant. The off-diagonal elements show that for both data sets there is considerable mixing between neutron events and the other classes. For the barrel data set there is also considerable mixing between photon and neutral pion events, since adding neutrons does not make the separation between photons and neutral pions any better.

6.4.2 Multivariate analysis

When including multiple parameters, the overlap with neutrons of the spectra of photons and neutral pions becomes less important and the separation efficiency between photons and neutral pions dominates. This conveniently results in the fact that the same combinations of parameters perform well as in the binary photon–neutral pion separation. The results of the parameter sets described earlier over the full momentum range are given in the table below.

Parameter	KNN	
	fw. end-cap	barrel
$\{E_{\text{cluster}}, \langle r_{\text{minor}}^2 \rangle\}$	0.964	0.826
$\{E_{\text{cluster}}, \langle r_{\text{minor}}^2 \rangle, f_{\text{max},4}\}$	0.974	0.893
$\{E_{\text{cluster}}, \langle r_{\text{minor}}^2 \rangle, f_{\text{max},4}, Z_5^3\}$	0.975	0.894

The complete confusion matrices for a KNN classification using the set of four parameters $\{E_{\text{cluster}}, \langle r_{\text{minor}}^2 \rangle, f_{\text{max},4}, Z_5^3\}$ are given by

$$M_{\text{fw. end-cap}} = \begin{pmatrix} 0.96 & 0.00 & 0.04 \\ 0.00 & 1.00 & 0.00 \\ 0.03 & 0.00 & 0.97 \end{pmatrix} \quad \text{and} \quad M_{\text{barrel}} = \begin{pmatrix} 0.85 & 0.11 & 0.04 \\ 0.10 & 0.89 & 0.01 \\ 0.03 & 0.02 & 0.95 \end{pmatrix}.$$

For the forward end-cap data set, the remaining misclassifications are mostly photons classified as neutrons and vice versa. The neutral pion events are more distinct and the chance of misclassifying them is less than 1%. For the barrel data set, the most important mixing occurs between photon and neutral pion events, with a mixing between photon and neutron events as the second most common source of misclassifications. The imperfect separation between photon and neutral pion events has obviously not improved.

This last section shows that adding neutrons to the photon–neutral pion classification problem does not extensively change which parameters perform well. When using the KNN algorithm, the same set of four parameters can be used to achieve reasonable results. To prevent the neutrons, which are relatively rare in the $\overline{\text{PANDA}}$ experiment, from negatively affecting the identification of photons and neutral pions, the classification routine could be tuned to only classify events as neutrons when they are very unlikely to belong to the other classes. However, this was not investigated.

Discussion and conclusions

During the annihilation events in the $\overline{\text{PANDA}}$ detector, large numbers of photons and neutral pions will be created. These neutral particles are detected by the particle showers they form in the electromagnetic calorimeter (EMC) of the detector, composed of lead–tungstate crystals (Chapter 1). The neutral pions decay immediately into mostly two photons. The two photons can have small opening angles for high-momentum pions, resulting in overlapping particle showers in the EMC (Chapter 2), which will be referred to as *two-photon clusters*. These clusters can be misinterpreted as showers stemming from single photons, referred to as *one-photon clusters*. Therefore, a method is required to differentiate between one-photon and two-photon clusters, which is the main objective of this thesis.

In this work, the PandaRoot simulation and analysis framework was used to simulate the response of the EMC of the $\overline{\text{PANDA}}$ detector using Monte Carlo techniques (Chapter 3). Several methods were described that allow the separation of one-photon and two-photon clusters in the EMC (Chapter 4). Using the GEANT3 transport model, the response of the forward end-cap and the barrel part of the EMC to photon and neutral pion events was simulated for momenta between 0 and 15 GeV/ c (Chapter 5). The results of these simulations were used to compare the various separation methods studied (Chapter 6).

The technique currently implemented in PandaRoot for handling multi-photon clusters is a ‘bump-splitting’ procedure, that consists of finding the (possibly multiple) maxima in a cluster and splitting the cluster accordingly (Section 3.2.3). This method can be used to identify clusters caused by the two photons due to a neutral pion decay, because in these cases there should be two maxima in the cluster, from which the correct invariant mass of the neutral pion can be reconstructed. However, this technique does not give perfect classification results (Section 6.1). The algorithm has difficulty separating maxima lying close together and this causes the invariant mass reconstruction to fail for a considerable fraction of high-momentum neutral pion events. Especially for the barrel part of the detector, the classification efficiency of the invariant mass reconstruction is limited, even when taking into account that the particles hitting the barrel part of the detector will generally be of lower momentum than those hitting the forward end-cap.

As an alternative to the bump-splitting procedure, several shower shape parameters were tested for their efficiency in classifying one-photon and two-photon clusters (Section 6.2). The best single parameter was determined to be the second lateral cluster moment, $\langle r^2 \rangle$, the energy-weighted average of the square of the distance to the cluster center (Section 4.3.3). While this parameter is simple to calculate, it gives very good results for both data sets. For the

forward end-cap, the separation using this parameter is essentially perfect over the full momentum range up to events of 15 GeV/ c . For the barrel data set, the separation efficiency is very good up to momenta of about 6 GeV/ c , but drops at higher momenta. However, events with higher momenta are rare for the barrel part of the detector and this separation efficiency is likely to be satisfactory.

A multivariate analysis was also performed for this work, using the KNN algorithm (Section 5.2.2). The results of this analysis show that a combination of up to four parameters can be used to slightly improve the classification results for the barrel part of the detector for momenta above 6 GeV/ c (Section 6.3). The strong correlation between the various shower shape parameters rules out any large improvements from using a multivariate data analysis. For the forward end-cap, the classification efficiency of several single parameters is already very good and using multiple parameters does not improve the results. Depending on the desired classification efficiency and the part of the EMC under consideration, the additional complexity of performing a multivariate analysis might outweigh the improvement of the classification efficiency.

It was not investigated whether it is possible to improve the bump-splitting procedure by optimizing its parameters or by changing the algorithm. A possibility that was not examined to improve the bump-splitting procedure is by using the shower shape parameters in the bump-splitting algorithm.

The addition of neutron events to the classification problem was also investigated in this work. It was found that the same parameters that provide good results for the separation between one-photon and two-photon events also work well in this case (Section 6.4). The reason for this is that neutrons form irregular clusters, resulting in wide distributions in all shower shape parameters investigated. The separation efficiency between photons and neutral pions remains therefore the most important factor in the overall separation efficiency.

An important process that was not included in this work is *external conversion*, where a photon is converted into an electron–positron pair in one of the inner subdetectors before reaching the EMC. The shower shapes of these events were not investigated and might form an important source of misclassified events. A similar analysis as performed in this work should be applied to the classification of this type of events, to investigate the role of shower shape parameters in such a classification problem.

To conclude, the separation between neutral pions and photons in the EMC of the $\overline{\text{P}}\text{ANDA}$ detector can be satisfactorily solved by using one or a combination of a small number of shower shape parameters. The currently implemented bump-splitting algorithm gives a lower separation efficiency than these shower shape parameters provide. The most important factor determining the final classification efficiency that will be achieved is the momentum distribution of particles, that depends on the part of the detector under consideration. The uniform momentum distribution that was used for simulations in this work is very unrealistic, but provides information on the momentum dependence of the classification results. More detailed knowledge of the expected momentum distributions during the actual experiment might allow a better judgment as to which parameters provide sufficient separation efficiency.

Bibliography

- [1] \bar{P} ANDA Collaboration, *Technical Design Report for \bar{P} ANDA Solenoid and Dipole Spectrometer Magnets* (2009)
arXiv:0907:0169.
- [2] \bar{P} ANDA Collaboration, *Technical Design Report for \bar{P} ANDA Electromagnetic Calorimeter (EMC)* (2008)
arXiv:0810.1216v1.
- [3] \bar{P} ANDA Collaboration, *Physics Performance Report* (2009)
arXiv:0903:3905v1.
- [4] ATLAS Collaboration, *Calorimeter Performance Technical Design Report* (1997), CERN/LHCC 94-40.
- [5] B. R. Martin, *Nuclear and Particle Physics — An Introduction*, Wiley, 1st edition (2006).
- [6] W. R. Leo, *Techniques for Nuclear and Particle Physics Experiments*, Springer-Verlag, 2nd edition (1994).
- [7] C. Amsler *et al.*, *Physics Letters* **B667**, 1 (2008).
- [8] M. Babai, *Pattern Recognition for Panda*, Master’s thesis, University of Groningen/KVI (2007).
- [9] C. Geldmann, *A Shower Analysis for the Electro-Magnetic Calorimeter of PANDA*, Bachelor’s thesis, Hochschule Bremen/KVI (2009).
- [10] S. Menke, *ATLAS Cluster Moments* (visited 2009)
<https://twiki.cern.ch/twiki/bin/view/Atlas/ClusterMoments>.
- [11] E. W. Weisstein, “Least Squares Fitting — Perpendicular Offsets” from *MathWorld* — A Wolfram Web Resource (visited 2009)
<http://mathworld.wolfram.com/LeastSquaresFittingPerpendicularOffsets.html>.
- [12] E. W. Weisstein, “Zernike Polynomial” from *MathWorld* — A Wolfram Web Resource (visited 2009)
<http://mathworld.wolfram.com/ZernikePolynomial.html>.

Appendix A

Additional data

This appendix gives the ROC integrals over three different momentum range for all parameters that have been described in Chapter 6. This provides some additional information about the momentum dependence of the parameters, most importantly for those that were not plotted in Chapter 6. The three momentum ranges are $p \in [2, 4]$ GeV/ c , $p \in [6, 8]$ GeV/ c and $p \in [10, 12]$ GeV/ c . The values for both the forward end-cap and the barrel data sets are given in each case.

Bump multiplicity

Parameter	p [GeV/ c]	ROC integral		
		2-4	6-8	10-12
n_{bumps}	fw. end-cap	0.992	0.984	0.960
	barrel	0.941	0.575	0.514
n_{bumps} ($E_{\text{threshold}} = 100$ MeV)		0.999	0.997	0.979
		0.949	0.577	0.513

Invariant mass reconstruction

Parameter	p [GeV/ c]	ROC integral		
		2-4	6-8	10-12
$m_{\text{invariant}}$	fw. end-cap	0.999	0.998	0.979
	barrel	0.948	0.578	0.515

Digi energy fractions

Parameter	p [GeV/ c]	ROC integral		
		2-4	6-8	10-12
$f_{\max,1} = f_{\square 1}$	fw. end-cap	0.924	0.837	0.806
	barrel	0.853	0.805	0.739
$f_{\max,2}$		0.913	0.908	0.897
		0.919	0.874	0.795
$f_{\max,3}$		0.958	0.958	0.954
		0.950	0.888	0.797
$f_{\max,4}$		0.994	0.997	0.996
		0.980	0.931	0.803
$f_{\max,5}$		0.996	0.995	0.993
		0.974	0.891	0.768
$f_{\max,6}$		0.996	0.995	0.993
		0.968	0.858	0.741
$f_{\square 9}$		1.000	0.999	0.999
		0.999	0.864	0.703
$f_{\square 25}$		1.000	0.999	0.993
		0.973	0.696	0.598
$E_{\square 1}/E_{\square 9}$		0.614	0.567	0.510
		0.519	0.770	0.733
$E_{\square 9}/E_{\square 25}$		0.512	0.753	0.910
		0.883	0.848	0.701
$E_{\square 1}/E_{\square 25}$		0.613	0.511	0.727
		0.716	0.800	0.738

Cluster mass

Parameter	p [GeV/ c]	ROC integral		
		2-4	6-8	10-12
m_{cluster}	fw. end-cap	1.000	0.999	0.997
	barrel	0.999	0.904	0.779

Cluster moments

Parameter	p [GeV/ c]	ROC integral		
		2-4	6-8	10-12
$\langle r \rangle$	fw. end-cap	1.000	0.999	0.992
	barrel	0.997	0.875	0.747
$\langle r^2 \rangle$		1.000	0.999	0.998
		1.000	0.946	0.807
$\langle \theta \rangle$		0.975	0.937	0.893
		0.908	0.757	0.673
$\langle \theta^2 \rangle$		0.984	0.949	0.921
		0.928	0.830	0.728
$\langle \phi \rangle$		0.976	0.948	0.911
		0.904	0.748	0.665
$\langle \phi^2 \rangle$		0.978	0.957	0.933
		0.926	0.819	0.720
normalized $\langle r \rangle$		0.999	0.988	0.964
		0.977	0.903	0.805
normalized $\langle r^2 \rangle$		1.000	0.999	0.991
		0.990	0.897	0.778

Zernike moments

Parameter	p [GeV/ c]	ROC integral		
		2-4	6-8	10-12
Z_2^0 ($\rho_0 = 15$ cm)	fw. end-cap	1.000	0.999	0.998
	barrel	1.000	0.944	0.801
Z_2^2 ($\rho_0 = 15$ cm)		1.000	0.999	0.997
		1.000	0.939	0.735
Z_3^1 ($\rho_0 = 15$ cm)		0.995	0.974	0.918
		0.919	0.619	0.525
Z_3^3 ($\rho_0 = 15$ cm)		0.999	0.990	0.966
		0.955	0.733	0.601
Z_4^0 ($\rho_0 = 15$ cm)		1.000	0.999	0.996
		0.999	0.943	0.804
Z_4^2 ($\rho_0 = 15$ cm)		0.999	0.992	0.986
		0.998	0.934	0.739
Z_4^4 ($\rho_0 = 15$ cm)		1.000	0.999	0.972
		0.960	0.643	0.545
Z_5^1 ($\rho_0 = 15$ cm)		0.981	0.973	0.927
		0.923	0.619	0.536
Z_5^3 ($\rho_0 = 15$ cm)		0.986	0.992	0.979
		0.968	0.802	0.674
Z_5^5 ($\rho_0 = 15$ cm)		0.999	0.977	0.856
		0.890	0.597	0.532

Eccentricity

Parameter	p [GeV/ c]	ROC integral		
		2–4	6–8	10–12
$\langle r_{\text{major}} \rangle$	fw. end-cap	0.726	0.738	0.744
	barrel	0.746	0.747	0.712
$\langle r_{\text{major}}^2 \rangle$		0.698	0.695	0.705
		0.731	0.734	0.710
$\langle r_{\text{minor}} \rangle$		1.000	0.999	0.994
		0.997	0.859	0.716
$\langle r_{\text{minor}}^2 \rangle$		1.000	0.999	0.998
		1.000	0.965	0.806
$\epsilon_{\text{cluster}}$		1.000	0.999	0.998
		0.998	0.871	0.670
$\mathfrak{J}_{\text{cluster}} (\Delta\rho = 1 \text{ cm})$		1.000	0.999	0.995
		0.994	0.892	0.683

Multivariate analysis

Parameter	p [GeV/ c]	KNN ROC integral		
		2–4	6–8	10–12
$\{E_{\text{cluster}}, \langle r_{\text{minor}}^2 \rangle\}$	fw. end-cap	1.000	1.000	1.000
	barrel	1.000	0.969	0.806
$\{E_{\text{cluster}}, \langle r_{\text{minor}}^2 \rangle, f_{\text{max}4}\}$		1.000	1.000	1.000
		1.000	0.984	0.890
$\{E_{\text{cluster}}, \langle r_{\text{minor}}^2 \rangle, f_{\text{max}4}, Z_5^3\}$		1.000	1.000	0.999
		1.000	0.986	0.894

Neutron – single parameters

Parameter	p [GeV/ c]	KNN		
		2–4	6–8	10–12
$f_{\text{max}4}$	fw. end-cap	0.757	0.899	0.920
	barrel	0.775	0.832	0.779
normalized $\langle r^2 \rangle$		0.765	0.790	0.877
		0.725	0.804	0.773
$\langle r_{\text{minor}}^2 \rangle$		0.870	0.894	0.850
		0.760	0.855	0.784
$\langle r^2 \rangle$		0.858	0.859	0.868
		0.746	0.838	0.792
m_{cluster}		0.877	0.898	0.910
		0.909	0.774	0.708
$\mathfrak{J}_{\text{cluster}} (\Delta\rho = 1 \text{ cm})$		0.749	0.845	0.841
		0.802	0.637	0.571
E_{cluster}		0.881	0.669	0.660
		0.676	0.672	0.668

Neutron – multivariate analysis

Parameter	p [GeV/c]	KNN		
		2-4	6-8	10-12
$\{E_{\text{cluster}}, \langle r_{\text{minor}}^2 \rangle\}$	fw. end-cap	0.998	0.999	0.999
	barrel	0.998	0.932	0.814
$\{E_{\text{cluster}}, \langle r_{\text{minor}}^2 \rangle, f_{\text{max}4}\}$		0.999	0.999	0.998
		0.998	0.955	0.872
$\{E_{\text{cluster}}, \langle r_{\text{minor}}^2 \rangle, f_{\text{max}4}, Z_5^3\}$		0.998	0.999	0.998
		0.997	0.957	0.873

